

Repulsive Sema3E-Plexin-D1 signaling coordinates both axonal extension and steering via activating an autoregulatory factor, Mtss1

Namsuk Kim^{1†}, Yan Li^{1†}, Ri Yu¹, Hyo-Shin Kwon¹, Anji Song¹, Mi-Hee Jun¹, Jin-Young Jeong^{1,2}, Ji Hyun Lee¹, Hyun-Ho Lim¹, Mi-Jin Kim³, Jung-Woong Kim³, Won-Jong Oh^{1*}

¹Neurovascular Unit Research Group, Korea Brain Research Institute, Daegu, Republic of Korea; ²Department of Brain and Cognitive Sciences, Daegu Gyeongbuk Institute of Science and Technology, Daegu, Republic of Korea; ³Department of Life Sciences, Chung-Ang University, Seoul, Republic of Korea

Abstract Axon guidance molecules are critical for neuronal pathfinding because they regulate directionality and growth pace during nervous system development. However, the molecular mechanisms coordinating proper axonal extension and turning are poorly understood. Here, metastasis suppressor 1 (Mtss1), a membrane protrusion protein, ensured axonal extension while sensitizing axons to the Semaphorin 3E (Sema3E)-Plexin-D1 repulsive cue. Sema3E-Plexin-D1 signaling enhanced Mtss1 expression in projecting striatonigral neurons. Mtss1 localized to the neurite axonal side and regulated neurite outgrowth in cultured neurons. Mtss1 also aided Plexin-D1 trafficking to the growth cone, where it signaled a repulsive cue to Sema3E. Mtss1 ablation reduced neurite extension and growth cone collapse in cultured neurons. *Mtss1*-knockout mice exhibited fewer striatonigral projections and irregular axonal routes, and these defects were recapitulated in *Plxnd1*- or *Sema3e*-knockout mice. These findings demonstrate that repulsive axon guidance activates an exquisite autoregulatory program coordinating both axonal extension and steering during neuronal pathfinding.

*For correspondence: ohwj@kbri.re.kr

†These authors contributed equally to this work

Competing interest: The authors declare that no competing interests exist.

Funding: See page 30

Preprinted: 04 May 2022

Received: 07 February 2024

Accepted: 14 March 2024

Published: 25 March 2024

Reviewing Editor: Jun Ding, Stanford University, United States

© Copyright Kim, Li et al. This article is distributed under the terms of the [Creative Commons Attribution License](https://creativecommons.org/licenses/by/4.0/), which permits unrestricted use and redistribution provided that the original author and source are credited.

Editor's evaluation

In this manuscript, the authors proposed a novel and attractive model to address a fundamental question of how the locational and function of axon guidance molecules are regulated. They presented convincing data to support their working model. They showed important findings that Sema3E-Plexin-D1 signaling regulates the expression of Mtss1, which regulates the localization of Plexin-D1 and contributes to striatonigral axonal growth and turning.

Introduction

In the developing nervous system, axons of newly generated neurons extend toward destination targets and make connections to establish a functional circuit following an exquisitely designed program. In this long-range pathfinding process, axons encounter attractive and repulsive signals from guidance molecules, and diverse combinations of ligand–receptor pairs communicate signals to a neuron from the environment (*Kolodkin and Tessier-Lavigne, 2011; Tessier-Lavigne and Goodman, 1996*). In addition to the conventional guidance mode, which has been established, recent studies

have demonstrated the complexity of signaling through different mechanistic layers, such as crosstalk between guidance molecules (Dupin et al., 2015; Poliak et al., 2015), guidance switching between different holoreceptor complexes (Bellon et al., 2010), or guidance tuning by intrinsic regulators (Bai et al., 2011; Bonanomi et al., 2019). In general, the specific cognate guidance receptors that sense extracellular signals are mostly localized in growth cones, a specialized structure at the fore of a growing axon, and these receptors convey intracellular signaling cues within neurons (Dent et al., 2011; Franze, 2020). Therefore, proper signaling from guidance molecules in the growth cone surface is critical as axons travel to their destination. Because the axonal destination can be as far as a meter or more away from the soma, various transport systems consisting of specific adaptors and motor proteins transport guidance proteins to axon terminals and are thus critical for axonal movement (Dent et al., 2011; Winckler and Mellman, 2010). However, how individual guidance molecules are correctly delivered to growth cones and can accommodate the axonal growth pace is unclear, and the molecular machinery critical for the specific transportation of guidance molecules is unknown.

Growth cones are highly dynamic and motile cellular structures that facilitate axon growth and steering through activated receptors that alter cytoskeletal actin and microtubule assembly (Lowery and Van Vactor, 2009; Vitriol and Zheng, 2012). Therefore, guidance receptors undoubtedly need to be localized to these protrusive structures to control actin dynamics. Since actin filament assembly is typically accompanied by membrane remodeling, a group of cytoskeletal scaffold proteins linking actin to the cell membrane must be activated (Vitriol and Zheng, 2012). One such protein group consists of Bin/Amphiphysin/Rvs (BAR) domain proteins, which have been implicated in many actin-associated membrane functions, such as cell motility, endocytosis, and organelle trafficking (Chen et al., 2013). Among these proteins, metastasis suppressor 1 (Mtss1, also called missing in metastasis), one of a few inverse BAR (I-BAR) domain subfamily proteins, is notable due to its capability of forming cellular protrusions by promoting inverse membrane curvature (Machesky and Johnston, 2007). Because of its unique ability to connect the plasma membrane inner leaflet with actin, the role of Mtss1 has been characterized in promoting spine protrusions as well as neuronal dendrite growth (Kawabata Galbraith et al., 2018; Saarikangas et al., 2015; Yu et al., 2016). However, in contrast to these many studies of Mtss1 on the dendritic side during development, few studies have investigated whether Mtss1 is expressed and plays a specific role in axons.

Semaphorin 3E (Sema3E), a class 3 secreted semaphorin family protein, conveys guidance signals by directly binding with the Plexin-D1 receptor in both the nervous and vascular systems (Gu et al., 2005; Oh and Gu, 2013a). The Sema3E-Plexin-D1 pair mainly transmits a repulsive guidance cue via local cytoskeletal changes, thereby inhibiting axonal overgrowth and/or ectopic synapse formation in the central nervous system (Chauvet et al., 2007; Ding et al., 2012; Fukuhara et al., 2013; Mata et al., 2018; Pecho-Vrieseling et al., 2009). Previous studies have demonstrated that Sema3E-Plexin-D1 signaling is involved in dendritic synapse formation as well as traditional axon projection in the basal ganglia circuitry, which is essential for diverse behavioral and cognitive functions in the brain (Ding et al., 2012; Ehrman et al., 2013). Notably, Plexin-D1 is expressed only in direct-pathway medium spiny neurons (MSNs) projecting to the substantia nigra pars reticulata (SNr), one of two distinct types of MSNs in the striatum (Ding et al., 2012). Plexin-D1-positive striatonigral axons travel through the corridor between the globus pallidus (Gp) and reticular thalamic nucleus (rTh)/zona incerta (ZI), in which Sema3E molecules reside and emit repulsive signals to direct proper pathway formation toward the SNr (Chauvet et al., 2007; Ehrman et al., 2013). However, how the striatonigral pathway coordinates axonal growth and steering during pathfinding remains largely unknown.

In this study, we investigated the molecular mechanism of the repulsive Sema3E-Plexin-D1 guidance signaling pair in striatonigral-projecting neurons during mouse basal ganglia circuit development. We found that Sema3E-Plexin-D1 signaling coordinates axonal extension and diversion by enhancing the action of the facilitator protein Mtss1 during active striatonigral projection progression. In the context of the important and intricate networks in the brain, this study provides evidence showing that autoregulatory factor expression regulated by guidance signaling leads to the correct neuronal trajectory to the destination.

Results

Sema3E-Plexin-D1 signaling regulates *Mtss1* expression in the developing striatum

The majority of striatal neurons are MSNs (up to 90%), and the MSNs are equally divided into direct and indirect pathways (Gerfen and Surmeier, 2011). In a previous study, we found that *Plxnd1* is selectively expressed in direct-pathway MSNs (also called striatonigral neurons) that project directly to the substantia nigra, with approximately 45% of striatal neurons identified as Plexin-D1-positive neurons (Ding et al., 2012). Because of the relative abundance of Plexin-D1-positive neurons, we expected a high probability of discovering the potential downstream responsive genes modulated by Sema3E-Plexin-D1 signaling in the striatum. Therefore, we performed bulk RNA sequencing (RNA-seq) with striatal tissues at P5, when *Plxnd1* expression is high in the striatum, and compared the results obtained with control (*Plxnd1*^{fl/fl}) and conditional neuronal *Plxnd1*-knockout (*Nes-Cre; Plxnd1*^{fl/fl}) mice (Figure 1A). *Plxnd1* mRNA ablation in striatal tissues was validated in pan-neuronal *Plxnd1*-knockout (*Nestin-Cre*) mice (Figure 1—figure supplement 1A and B).

Next, we performed gene expression profile analysis. The principal component analysis (PCA) plot showed that *Plxnd1*-knockout accounted for the largest variance, and the results obtained in biological replicates showed high reproducibility (Figure 1—figure supplement 1C). Application of a conservative DEseq approach to RNA-seq data analysis confirmed 2360 differentially expressed transcripts (Figure 1—figure supplement 1D). Gene Ontology (GO) analysis was then performed, and biological connections between upregulated (1240 transcripts) and downregulated (1120 transcripts) differentially expressed genes (DEGs) in *Plxnd1*-knockout mice compared to wild-type (control) mice were identified (Figure 1—figure supplement 1E). Clustering of the downregulated DEGs in *Plxnd1*-knockout mice enabled their classification into several categories that were associated with axon guidance, regulation of dendritic spine morphology, and neuronal projection. The volcano plots present the statistical significance of differential transcript expression with the respective fold change values ($p < 0.05$, absolute \log_2 [fold change, FC] > 1) compared to the expression observed in the control group (Figure 1B).

Among the downregulated genes, *Mtss1* was particularly notable due to its high relevance to actin cytoskeletal rearrangement (Kawabata Galbraith et al., 2018; Lin et al., 2005; Saarikangas et al., 2015). *Mtss1* gene expression was verified by quantitative RT-PCR (qRT-PCR) performed with *Plxnd1*-knockout striatal tissues (Figure 1C). The *Mtss1* protein levels were also markedly decreased in the knockout mice at P5 (Figure 1D and E). We also analyzed *Mtss1* expression in *Sema3e*-knockout striatal samples obtained at P5 and found that its expression was decreased, but less dramatically than it was in *Plxnd1*-knockout striatal samples (Figure 1F and G). These results suggest that Sema3E-Plexin-D1 signaling activation can increase *Mtss1* expression in striatal neurons during development.

Mtss1 is selectively expressed in striatonigral-projecting neurons during the active pathfinding period

To determine whether this *Mtss1* expression is specific to Plexin-D1-positive neurons, we first performed fluorescence in situ hybridization. *Mtss1* expression significantly overlapped with *Plxnd1*-positive neurons in both the cortex and striatum, and its expression was reduced in *Plxnd1*-knockout mice (Figure 1H and I). Moreover, when we performed immunostaining with *Drd1a*-tdT mice, in which direct-pathway MSNs fluoresced red (Ade et al., 2011), *Mtss1* expression significantly overlapped with *Drd1a*-tdT striatal neurons (Figure 1J; $98.2 \pm 1.72\%$), suggesting that Plexin-D1 signaling mediates *Mtss1* expression selectively in striatonigral projecting MSNs. Although *Mtss1* was expressed at a low level regardless of Plexin-D1 presence at E16.5, it seemed to be under the control of Plexin-D1 signaling in the developing striatum from the last gestation period to the early postnatal period (Figure 1K and L). Furthermore, the Sema3E ligand activating the Plexin-D1 receptor was predominantly expressed in the thalamus and released into the striatum, probably during thalamostriatal projection at E16.5, as observed in the early postnatal stage in a previous study (Figure 1—figure supplement 2; Ding et al., 2012). Next, we analyzed the expression profiles of Plexin-D1 and *Mtss1* from the developmental stage to the adult stage. Both Plexin-D1 and *Mtss1* were expressed in the embryonic striatum, and their expression was elevated in the perinatal stage. Interestingly, *Mtss1* expression was maintained at a relatively high level from E18.5 to P5 and then declined sharply and

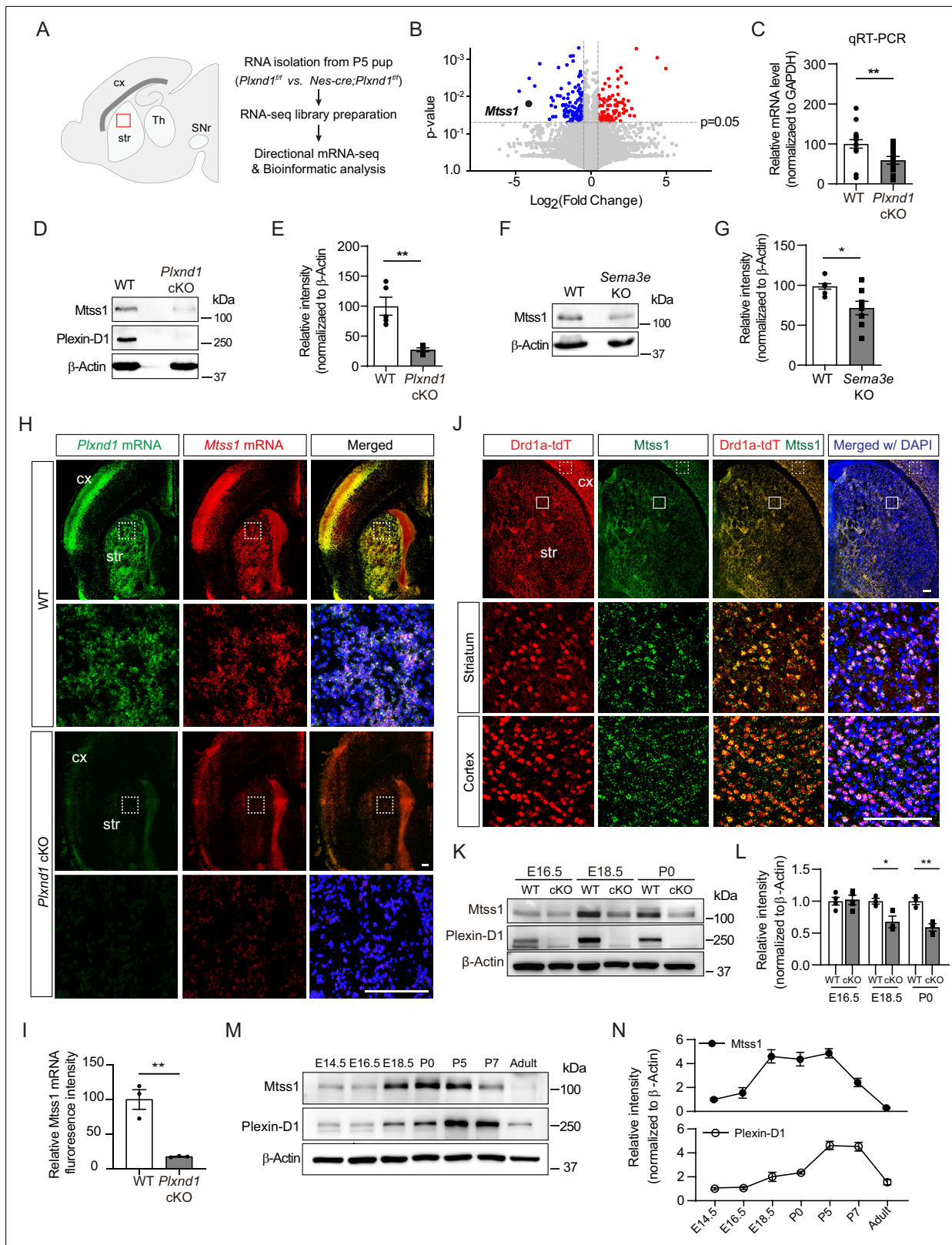


Figure 1. Sema3E-Plexin-D1 signaling induces *Mtss1* expression selectively in developing striatonigral projecting neurons. **(A)** RNA sequencing (RNA-seq) analysis of wild-type (WT) (*Plxnd1*^{+/+}) and conditional neuronal knockout (cKO) (*Nes-cre; Plxnd1*^{+/Δ}) pups at P5. The box in red indicates the dorsal striatum region from which RNA was isolated. **(B)** Volcano plot of significant differentially expressed genes (DEGs) between WT and *Plxnd1* cKO. Blue and red circles indicate significantly down- and upregulated genes, respectively, as indicated by a fold change greater than 2. **(C)** Relative levels of *Mtss1* mRNA in WT and *Plxnd1* cKO pups. **(D)** Western blot analysis of *Mtss1*, Plexin-D1, and β-Actin in WT and *Plxnd1* cKO pups. **(E)** Relative levels of *Mtss1* protein in WT and *Plxnd1* cKO pups. **(F)** Western blot analysis of *Mtss1* and β-Actin in WT and *Sema3e* KO pups. **(G)** Relative levels of *Mtss1* protein in WT and *Sema3e* KO pups. **(H)** Immunofluorescence images showing *Plxnd1* mRNA (green), *Mtss1* mRNA (red), and merged images in WT and *Plxnd1* cKO pups. **(I)** Relative levels of *Mtss1* mRNA fluorescence intensity in WT and *Plxnd1* cKO pups. **(J)** Immunofluorescence images showing Drd1a-tdT (red), *Mtss1* (green), merged images, and DAPI (blue) in WT and *Plxnd1* cKO pups. **(K)** Western blot analysis of *Mtss1*, Plexin-D1, and β-Actin in WT and cKO pups at E16.5, E18.5, and P0. **(L)** Relative levels of *Mtss1* protein in WT and cKO pups at E16.5, E18.5, and P0. **(M)** Western blot analysis of *Mtss1*, Plexin-D1, and β-Actin in WT and cKO pups at E14.5, E16.5, E18.5, P0, P5, P7, and Adult. **(N)** Relative levels of *Mtss1* and Plexin-D1 protein in WT and cKO pups over time from E14.5 to Adult.

Figure 1 continued on next page

Figure 1 continued

of *Mtss1* expression in the striatum of WT or *Plxnd1* cKO mice at P5 were compared by quantitative RT-PCR (RT-qPCR). $n = 16$ for WT mice, $n = 14$ for *Plxnd1* cKO mice in four independent experiments. (D, E) Western blot images showing *Mtss1* expression in the striatum of WT or *Plxnd1* cKO mice and quantification. The values are averaged from $n = 5$ for WT mice and $n = 4$ for *Plxnd1* cKO mice. (F, G) Western blot images and quantification of *Mtss1* expression in the striatum of WT or *Sema3e* KO mice at P5. WT mice, $n = 7$, and *Sema3e* KO mice, $n = 8$. (H) Fluorescence in situ hybridization (FISH) for *Plxnd1* mRNA (green) and *Mtss1* mRNA (red) in the striatum of WT or *Plxnd1* cKO mice at P5. White dotted boxes are shown in the inset image on the bottom. Scale bar, 200 μm . (I) Quantification of fluorescence intensity to measure the expression levels of *Mtss1* in (H). WT mice, $n = 3$, and *Plxnd1* cKO mice, $n = 3$. (J) Immunohistochemistry showing tdTomato-expressing *Drd1a*+MSNs (red) and *Mtss1* (green) in the striatum of *Drd1a*-tdT mice at P5. The small boxes in the striatum and cortex are shown at better resolution in the inset images. Scale bar, 100 μm . (K) Western blot images showing the expression of *Mtss1* and Plexin-D1 in the striatum of WT or *Plxnd1* cKO mice at different developmental stages ranging from embryonic day 16.5 (E16.5) to postnatal day 0 (P0). (L) Quantification of band intensity in (K). WT, $n = 4$, and KO, $n = 4$ at E16.5, WT, $n = 3$, and KO, $n = 3$ at E18.5, WT, $n = 3$, and KO, $n = 3$ at P0. (M, N) Western blot images showing the temporal expression of Plexin-D1 and *Mtss1* in the striatum from E14.5 to adulthood (8 weeks old) and quantification. Error bars, mean \pm SEM; * $p < 0.05$, ** $p < 0.01$ by Student's t-test for all quantifications. The values represent the average band intensity, $n = 3$ at each age. str, striatum; cx, cortex; Th, thalamus; SNr, substantia nigra.

The online version of this article includes the following source data and figure supplement(s) for figure 1:

Source data 1. Western blots shown in **Figure 1D, F, K, and M**.

Figure supplement 1. Identification of *Mtss1* in the striatum on P5 through RNA sequencing (RNA-seq) analysis.

Figure supplement 1—source data 1. RT-PCR shown in **Figure 1—figure supplement 1B**.

Figure supplement 2. *Sema3E* expression through thalamostriatal projections at E16.5.

Figure supplement 2—source data 1. Western blots shown in **Figure 1—figure supplement 2C**.

disappeared in the adult striatum, and although Plexin-D1 showed a similar expression pattern, its expression was maintained at a low level in the adult striatum, presumably to regulate other functions such as thalamostriatal synapse formation (**Figure 1M and N**; [Ding et al., 2012](#)).

Sema3E-Plexin-D1 signaling regulates *Mtss1* expression in cultured medium spiny neurons

To determine whether Plexin-D1-driven *Mtss1* expression can be recapitulated in vitro, we compared the *Mtss1* levels in cultured striatal neurons isolated from wild-type and *Plxnd1*-null mice. In wild-type neurons, both Plexin-D1 and *Mtss1* expression levels were low at day 3 in vitro (DIV3) and then increased by DIV6. In contrast, *Plxnd1*-knockout neurons failed to elevate *Mtss1* expression by DIV6, suggesting that *Mtss1* expression is induced at the cellular level rather than by indirect systemic changes at the circuit level in vivo (**Figure 2A and B**). In addition, the expression of *Mtss1* was decreased in cultured *Sema3e*-knockout neurons (**Figure 2C and D**). Next, to further confirm that the *Sema3E*-Plexin-D1 guidance pair is required for the activation of *Mtss1* expression in striatonigral neurons, we supplemented the *Sema3e*- or *Plxnd1*-knockout neurons with exogenous *Sema3E* ligand according to the scheme in **Figure 2E**. Given that some *Sema3E* ligands are naturally present in our striatal cultures from globus pallidus neurons, conducting tests on the exogenous *Sema3E* effect in the *Sema3e*-knockout cultures is ideal to minimize experimental variation. In fact, *Mtss1* expression was increased by *Sema3E* replenishment in *Sema3e*-knockout neurons, whereas it was not altered in *Plxnd1*-knockout neurons (**Figure 2F–I**). Moreover, since Akt is already known to mediate the *Sema3E*-Plexin-D1 signaling cascade in neurons ([Burk et al., 2017](#)), we next examined whether disturbing Akt activity alters *Mtss1* expression in cultured neurons. Treatment with an Akt inhibitor, MK2206, down-regulated *Mtss1* expression but caused no changes in Plexin-D1 levels (**Figure 2J–M**). Furthermore, the elevated expression of *Mtss1* due to the addition of exogenous *Sema3E* supplement in *Sema3e*-knockout neurons was also diminished by MK2206, suggesting that the *Sema3E*-Plexin-D1 pathway is involved in *Mtss1* expression through Akt signaling (**Figure 2N and O**). These results suggest that *Mtss1* is a downstream expression target of *Sema3E*-Plexin-D1 signaling in direct-pathway MSNs.

Mtss1 is important for neurite extension in direct-pathway MSNs

Since *Mtss1* has a well-characterized role in the regulation of filopodia and spine precursors ([Saarikangas et al., 2015](#); [Yu et al., 2016](#)), we first tested the morphological changes induced by *Mtss1* in COS7 cells. *Mtss1* was weakly expressed in COS7 cells, but its levels were not altered after over-expressing Plexin-D1 with or without *Sema3E* (**Figure 3—figure supplement 1A and B**). *Mtss1*

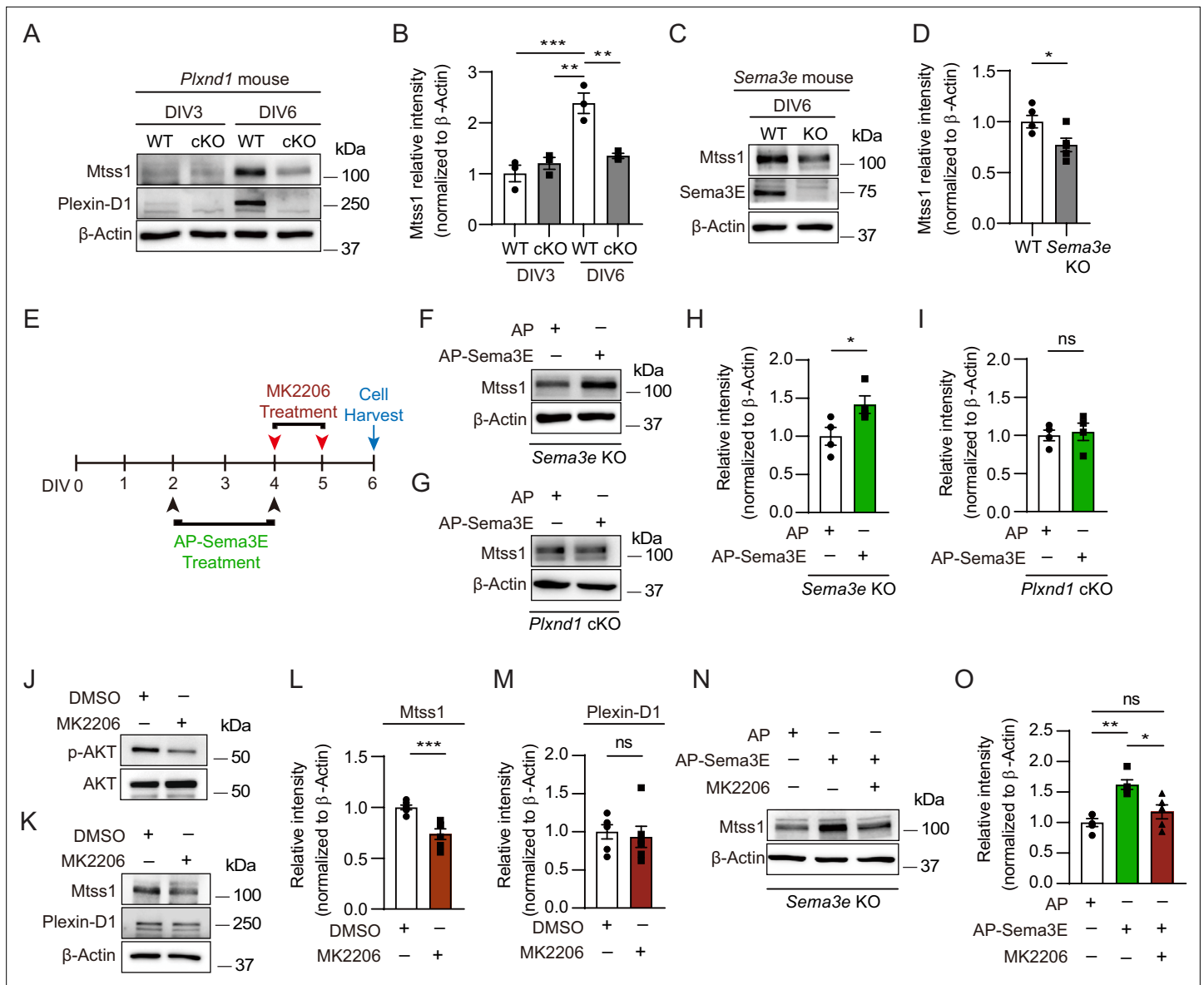


Figure 2. In cultured medium spiny neurons (MSNs), Mtss1 expression is directly regulated by Sema3E-Plexin-D1 signaling through the AKT pathway. (A) Western blot images showing Mtss1 expression in MSNs derived from the striatum of wild-type (WT) or *Plxnd1* conditional knockout (cKO) mice at P0 and measured at DIV3 and DIV6 in culture. (B) Quantification of band intensity in (A). Two-way ANOVA with Tukey's post hoc correction for multiple comparisons; $n = 3$. (C) Mtss1 expression in MSNs obtained from the striatum of WT or *Sema3e* KO mice at P0 and measured at DIV6 in culture. (D) Quantification of the blots shown in (C). Student's *t*-test; $n = 5$ for WT, $n = 5$ for KO in five independent experiments. (E) Schematic illustration of the experimental strategy for Sema3E-ligand or MK2206, an AKT inhibitor treatment in MSN culture. (F, G) Western blot images showing Mtss1 expression after AP-Sema3E (2 nM) treatment in cultured MSNs derived from *Sema3e* KO mice or *Plxnd1* cKO mice. (H, I) Quantification of (F, G). Student's *t*-test; AP, $n = 4$, AP-Sema3E, $n = 4$ for *Sema3e* KO mice, AP, $n = 4$, AP-Sema3E, $n = 4$ for *Plxnd1* cKO mice in three independent experiments. (J, K) Western blot to analyze the expression of Mtss1 and Plexin-D1 after MK2206 (100 nM) treatment in cultured MSNs and subsequent quantification for band intensity (L, M). Student's *t*-test; $n = 6$ for sham, $n = 6$ for MK2206 in six independent experiments. (N, O) Western blot image and analysis showing Mtss1 expression in *Sema3e* knockout MSNs treated with MK2206 after incubation with AP-Sema3E. Two-way ANOVA with Tukey's post hoc correction for multiple comparisons; $n = 5$ in five independent experiments. Error bars, mean \pm SEM; * $p < 0.05$, ** $p < 0.01$, *** $p < 0.001$ by indicated statistical tests.

The online version of this article includes the following source data for figure 2:

Source data 1. Western blots shown in Figure 2A, C, F, G, J, K, and N.

overexpression in COS7 cells led to a diverse degree of morphological changes, such as excessively spiky or thin and long processes, and highly localized in F-actin-enriched protrusions. However, overexpression of Mtss1 lacking the I-BAR domain failed to generate these protrusive shapes (**Figure 3—figure supplement 1C and D**). Mtss1 lacking WH2 domain showed much weaker effect because WH2 is an important region for Mtss1 interaction with F-actin (*Mattila et al., 2003*). These results suggest that Mtss1 is involved in F-actin dynamics and thus may be an important regulator of neurite outgrowth in cultured MSNs, similar to the situations in other types of neurons (*Kawabata Galbraith et al., 2018; Saarikangas et al., 2015; Yu et al., 2016*).

Interestingly, Mtss1 was significantly localized to the Tau-positive-axonal side of cultured MSNs at DIV3 (**Figure 3A**). We measured the neurite length of the direct-pathway MSNs that had been genetically labeled with red fluorescence in *Drd1a*-tdT crossbred reporter mice. We observed significant growth retardation in MSNs lacking *Mtss1* compared to wild-type neurons at DIV3 and DIV6 (**Figure 3B, C and E, F**). Furthermore, we also observed that *Mtss1*-deficient neurons failed to extend neurites more than twice the size of the cell body, suggesting that a lack of *Mtss1* presumably caused a severe neurite growth defect (**Figure 3D**). Next, we analyzed neurite length in *Plxnd1*-knockout neurons. Interestingly, there was no difference in neurite length between *Drd1a*-positive wild-type MSNs and *Plxnd1*-knockout MSNs at DIV3 (**Figure 3G and H**), probably due to the low Mtss1 induction shown in **Figure 2A**, whereas the length was significantly reduced in the *Plxnd1*-deficient MSNs at DIV6 (**Figure 3I and J**). These results suggest the possibility that Mtss1 expression is independent of Plexin-D1 signaling in the young neurons as observed in early development (**Figure 1K**). However, Mtss1 expression appears to be highly induced by *Sema3E*-Plexin-D1 activation to regulate axonal extension as neurons mature. To further confirm that low Mtss1 expression is critical for shortening neurite outgrowth, we overexpressed Mtss1 in *Plxnd1*-deficient MSNs. In comparison to the neurite length observed in GFP-overexpressing MSNs, ectopic Mtss1 overexpression rescued the growth reduction phenotype in the *Plxnd1*-knockout neurons (**Figure 3K and L**). These results suggest that the *Sema3E*-Plexin-D1 repulsive guidance cue is capable of regulating axonal growth through positive facilitator proteins such as Mtss1.

The Mtss1 I-BAR domain binds to Plexin-D1, and this interaction is *Sema3E*-independent

Since both Plexin-D1 and Mtss1 regulate actin cytoskeletal rearrangement as a guidance molecule and membrane transformer, respectively, near the cell surface, we speculated that Plexin-D1 and Mtss1 might interact with each other via the BAR domain to induce actin-related cellular events. To test whether Plexin-D1 and Mtss1 can physically interact, we generated multiple deletion constructs of human Plexin-D1 and Mtss1 (**Figure 4A**). When we overexpressed full-length Plexin-D1 and Mtss1 together in HEK293T cells, both proteins were successfully pulled down together (**Figure 4B**). However, Plexin-D1 with the intracellular domain (ICD) deleted failed to bind Mtss1, indicating an intracellular Plexin-D1 and Mtss1 interaction (**Figure 4C**). When we overexpressed full-length Plexin-D1 and each Mtss1 deletion construct, every Mtss1 construct containing the I-BAR domain coprecipitated with Plexin-D1, but I-BAR-deficient Mtss1 failed to interact with Plexin-D1 (**Figure 4D**). In a previous study, it was determined that Plexin-D1 interacts with SH3-domain binding protein 1 (SH3BP1), another protein of the BAR domain family (*Tata et al., 2014*), thus we investigated whether Plexin-D1 also binds to other BAR domain-containing proteins in general. As previously reported, we found that overexpression of Plexin-D1 in HEK293T cells resulted in the formation of a complex with overexpressed SH3BP1 (**Figure 4—figure supplement 1A**). However, it did not form a complex with srGAP2, a protein containing an F-BAR domain, or IRSP53, another protein containing an I-BAR domain like Mtss1 (**Figure 4—figure supplement 1B and C**). Conversely, we also examined whether Mtss1 can interact with other members of the Plexin family. As shown in **Figure 4—figure supplement 1D and E**, overexpressed Mtss1 was unable to form a complex with Plexin-B2 or -B3 proteins. These findings suggest that the formation of the Plexin-D1-Mtss1 complex is relatively specific.

Since *Sema3E* binding to Plexin-D1 caused SH3BP1 release from the complex (*Tata et al., 2014*), we examined whether *Sema3E* binding influences Mtss1 dissociation from Plexin-D1. In contrast to the effect on SH3BP1, *Sema3E* treatment did not interfere with Plexin-D1-Mtss1 complex formation, indicating that the complex is formed in a *Sema3E*-independent manner (**Figure 4E and F**). Moreover, to determine whether Plexin-D1 and Mtss1 can bind directly to each other, we performed an in vitro

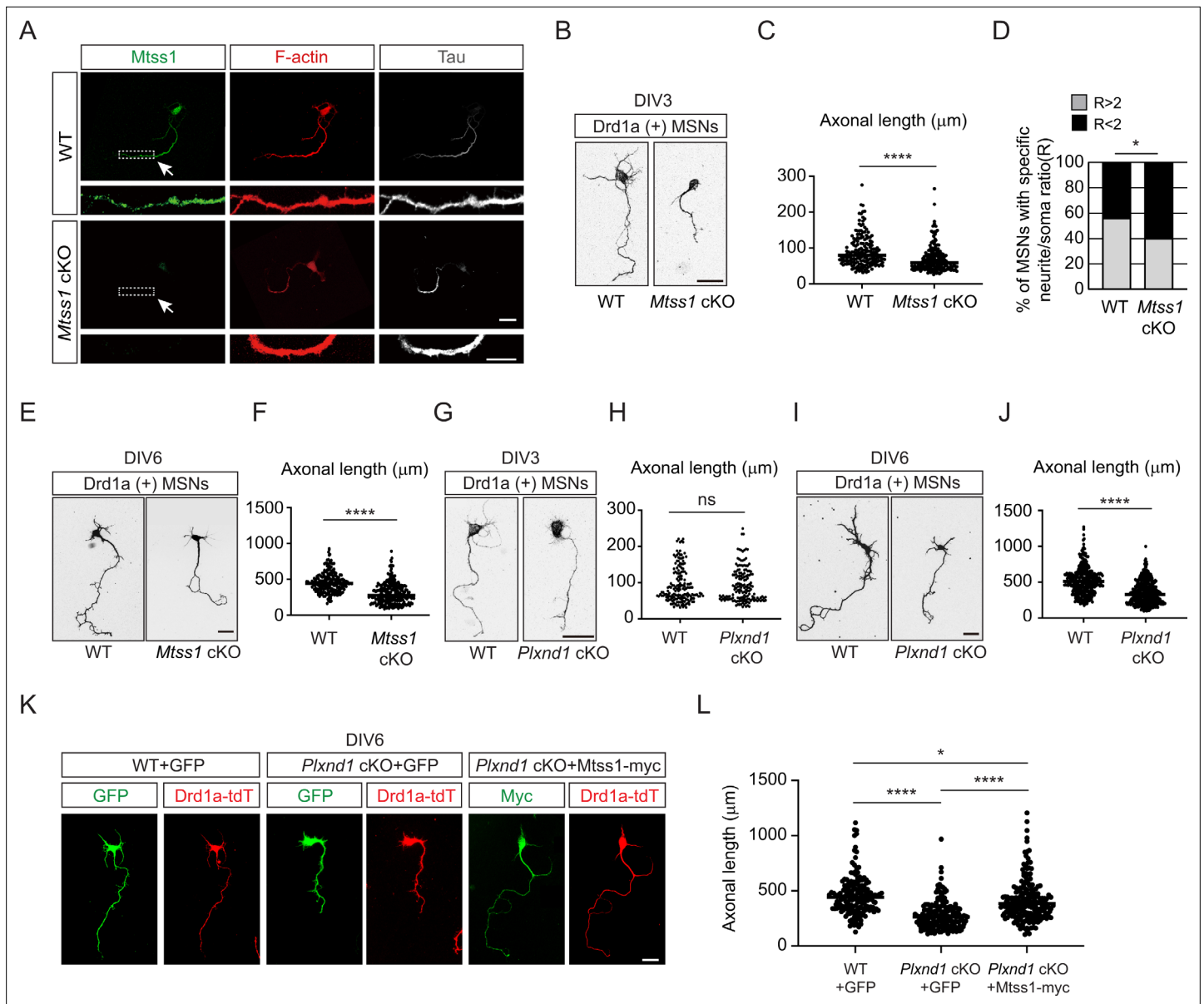


Figure 3. *Mtss1* contributes to neurite extension of *Drd1a*-positive medium spiny neurons (MSNs) under the regulation of Sema3E-Plexin-D1 signaling. **(A)** Immunocytochemistry for *Mtss1* (green), Tau (gray), and F-actin (red) in cultured MSNs at DIV3 obtained from wild-type (WT) or *Mtss1* conditional knockout (cKO) mice. White dotted boxes are shown in the inset image on the bottom. Scale bar, 10 μ m. **(B)** Representative images of *Drd1a*+MSNs at DIV3 derived from WT (*Drd1a*-tdT; *Mtss1*^{fl/y}) or *Mtss1* cKO (*Drd1a*-tdT; *Nes*-cre; *Mtss1*^{fl/y}) mice. Scale bar, 20 μ m. **(C)** Quantification of neurite length in **(B)** was performed as previously reported (Chauvet et al., 2016). The values represent the average ratio of the fold change in length compared to the control samples. Student's *t*-test; *n* = 179 for WT, *n* = 184 for *Mtss1* cKO, in three independent experiments. **(D)** Percentage of *Drd1a*-positive MSNs with neurites shorter than twice the cell body diameter in **(B, C)**. χ^2 test; *n* = 48 for WT, *n* = 48 for *Mtss1* cKO in four independent experiments. **(E)** Representative images of *Drd1a*+MSNs at DIV6 derived from WT (*Drd1a*-tdT; *Mtss1*^{fl/y}) or *Mtss1* cKO (*Drd1a*-tdT; *Nes*-cre; *Mtss1*^{fl/y}) mice. Scale bar, 50 μ m. **(F)** Quantification of neurite length in **(E)**. Student's *t*-test; *n* = 210 for WT, *n* = 260 for *Mtss1* cKO in three independent experiments. **(G)** Representative images of *Drd1a*+MSNs at DIV3 derived from WT (*Drd1a*-tdT; *Plxnd1*^{fl/y}) or *Plxnd1* cKO (*Drd1a*-tdT; *Nes*-cre; *Plxnd1*^{fl/y}) mice. Scale bar, 20 μ m. **(H)** Quantification of neurite length in **(G)**. Student's *t*-test; *n* = 167 for WT, *n* = 159 for *Plxnd1* cKO in three independent experiments. **(I)** Representative images of *Drd1a*+MSNs at DIV6 derived from WT or *Plxnd1* cKO mice. Scale bar, 50 μ m. **(J)** Quantification of neurite length in **(I)**. Student's *t*-test; *n* = 339 for WT, *n* = 403 for *Plxnd1* cKO in three independent experiments. **(K)** Representative images of GFP- or *Mtss1*-myc-transfected-*Drd1a*+MSNs at DIV6 derived from WT or *Plxnd1* cKO mice. Scale bar, 50 μ m. **(L)** Quantification of neurite length in **(K)**. Error bars, mean \pm SEM; **p*<0.05, *****p*<0.0001 by one-way ANOVA with Tukey's post hoc correction for multiple comparisons; *n* = 163 for WT + GFP, *n* = 187 for *Plxnd1* cKO + GFP, *n* = 195 for *Plxnd1* cKO + *Mtss1*-myc in three independent experiments. Error bars, mean \pm SEM; ns *p*>0.05, **p*<0.05, *****p*<0.0001 by indicated statistical tests.

Figure 3 continued on next page

Figure 3 continued

The online version of this article includes the following source data and figure supplement(s) for figure 3:

Figure supplement 1. Expression of Mtss1 induces I-BAR domain-dependent morphological changes in COS7 cells, generating protrusions.

Figure supplement 1—source data 1. Western blots shown in **Figure 3—figure supplement 1A**.

protein–protein binding assay using the purified ICD of Plexin-D1 and the I-BAR domain of Mtss1 proteins. As shown in **Figure 4G**, both proteins precipitated together, suggesting that Plexin-D1 and Mtss1 play a role as direct binding partners.

Mtss1 transports Plexin-D1 to the growth cone in cultured direct-pathway MSNs

Because of the high probability of localization of the Plexin-D1-Mtss1 complex at the cell membrane, Mtss1 may regulate Plexin-D1 function at the cell surface. To investigate the role of Mtss1 in Plexin-D1 activity, we first examined whether Mtss1 affects the Plexin-D1 level on the plasma membrane by performing a surface molecule biotinylation analysis. We observed that overexpressed Plexin-D1 proteins in COS7 cells were efficiently biotinylated on the cell surface, but the Plexin-D1 protein level on the surface was not changed during Mtss1 coexpression (**Figure 5—figure supplement 1A and B**). Another potential mechanism by which Mtss1 may affect Plexin-D1 activity might be endocytic regulation because Plexin-D1 is rapidly endocytosed after Semaphorin 3E treatment (**Burk et al., 2017**). However, Mtss1 coexpression did not affect Semaphorin 3E-induced Plexin-D1 endocytosis (**Figure 5—figure supplement 1C and D**). Additionally, Mtss1 overexpression did not change the binding affinity of Semaphorin 3E for Plexin-D1 (**Figure 5—figure supplement 1E**). These data, including those regarding Semaphorin 3E-independent complex formation (**Figure 4E and F**), suggest that Mtss1 does not directly affect the functional role of Semaphorin 3E-Plexin-D1 at the cell-surface level.

We next hypothesized that Mtss1 forms a complex with Plexin-D1 that targets Plexin-D1 to filopodium-like structures since we observed that Mtss1 is mainly involved in protrusion formation and neurite outgrowth in cultured cells. To test this possibility, we coexpressed Plexin-D1 and Mtss1 and analyzed their localization in COS7 cells. As shown in **Figure 5—figure supplement 1F and G**, when Plexin-D1 and Mtss1 were coexpressed, both proteins were mostly present in F-actin-enriched protrusions. However, overexpression of Plexin-D1 lacking the ICD overlapped with Mtss1 to a lesser extent than overexpression of wild-type Plexin-D1, whereas Mtss1 was abundant in the protrusions. In addition, Mtss1 lacking the I-BAR domain, which possesses membrane-bending activity, did not generate filopodia-like protrusions in COS7 cells but was localized with F-actin, including in marginal areas, probably via the Mtss1 WH2 domain (**Mattila et al., 2003**). Interestingly, although Plexin-D1 was evenly distributed throughout a cell, most Plexin-D1 was not present with Mtss1 missing the I-BAR domain. In addition, the localization of Plexin-D1 and Mtss1 in the protrusions was also not disturbed in the presence of Semaphorin 3E (**Figure 5—figure supplement 1H**). These results suggest that Mtss1 not only induces cell protrusion formation but also contributes to Plexin-D1 localization to specific sites.

Next, to confirm that Mtss1 leads Plexin-D1 to protrusive structures, such as growth cones in cultured neurons, Mtss1 and Plexin-D1 localization was analyzed by transfecting Mtss1-deficient striatal neurons with expression constructs carrying both proteins. Both overexpressed Plexin-D1 and Mtss1 proteins seemed to be colocalized along growing neurites, but the Mtss1 mutant lacking the I-BAR domain showed reduced Plexin-D1 level as well as a low colocalization rate (**Figure 5A–C**). As shown in COS7 cells (**Figure 5—figure supplement 1F**), wild-type Mtss1 proteins were present with Plexin-D1 in F-actin-enriched regions of growth cones; in contrast, mutant Mtss1 was expressed at a lower level than wild-type Mtss1 and failed to colocalize with Plexin-D1, resulting in reduced Plexin-D1 localization in the growth cone (**Figure 5D–F**). However, the intensity of Plexin-D1 upon co-expression of wild-type Mtss1 or mutant Mtss1 remained unchanged in the cell body (**Figure 5—figure supplement 2A and B**). It is plausible that overexpressed proteins accumulate in the soma, and a limited proportion of them are destined to the axon terminal on demand (**Droz et al., 1973**). To explore the role of Mtss1 in transporting Plexin-D1, we directly monitored the movement of Plexin-D1 along neurites in real time by imaging Drd1a-positive MSNs expressing Plexin-D1-GFP fusion proteins in wild-type and Mtss1-knockout neurons at DIV6. Our live-cell imaging showed that the majority of Plexin-D1-containing vesicles were dynamically transported in both proximal and distal

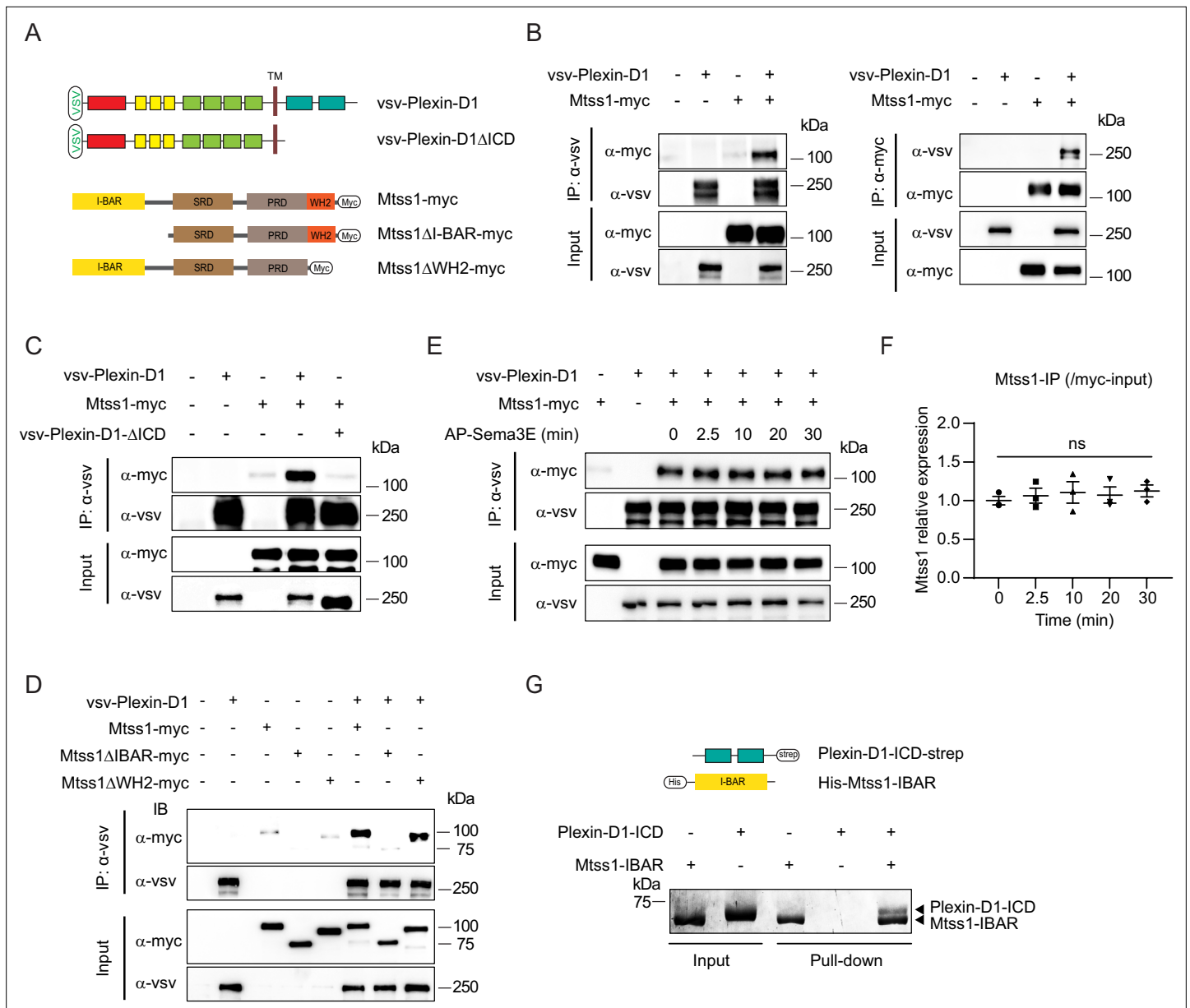


Figure 4. The Mtss1 I-BAR domain directly binds to Plexin-D1, independent of Sema3E. **(A)** Schematics depicting full-length constructs of Mtss1 and its truncation mutants. **(B)** Coimmunoprecipitation and immunoblot analysis of HEK293T cells transfected with Mtss1-myc with vsv-Plexin-D1. The interaction between Mtss1 and Plexin-D1 was investigated by immunoprecipitation with anti-vsv (left) or anti-myc (right) antibodies and subsequent western blotting with reciprocal antibodies. **(C)** Immunoprecipitation and western blot analysis after Plexin-D1 and Mtss1 overexpression. The vsv-Plexin-D1ΔICD did not bind to Mtss1-myc. **(D)** Immunoprecipitation and western blot assays to identify the binding domain in Mtss1 that interacts with Plexin-D1. **(E)** The interaction between Mtss1 and Plexin-D1 was assessed over time following treatment with Sema3E (2 nM) and was not affected by AP-Sema3E treatment. **(F)** Graph quantifying the band intensity in **(E)**. Error bars, mean ± SEM; ns $p > 0.05$ by two-way ANOVA with Bonferroni's post hoc correction for multiple comparisons; $n = 3$ in three independent experiments. **(G)** Pull-down assay and visualization of the protein bands using Coomassie staining. His-Mtss1-IBAR binds directly to Plexin-D1-ICD-strep.

The online version of this article includes the following source data and figure supplement(s) for figure 4:

Source data 1. Western blots and gel shown in **Figure 4B, C, D, E, and G**.

Figure supplement 1. The interaction between BAR domain-containing proteins and Plexin-D1, or between Mtss1 and Plexin family proteins.

Figure supplement 1—source data 1. Western blots shown in **Figure 4—figure supplement 1A–E**.

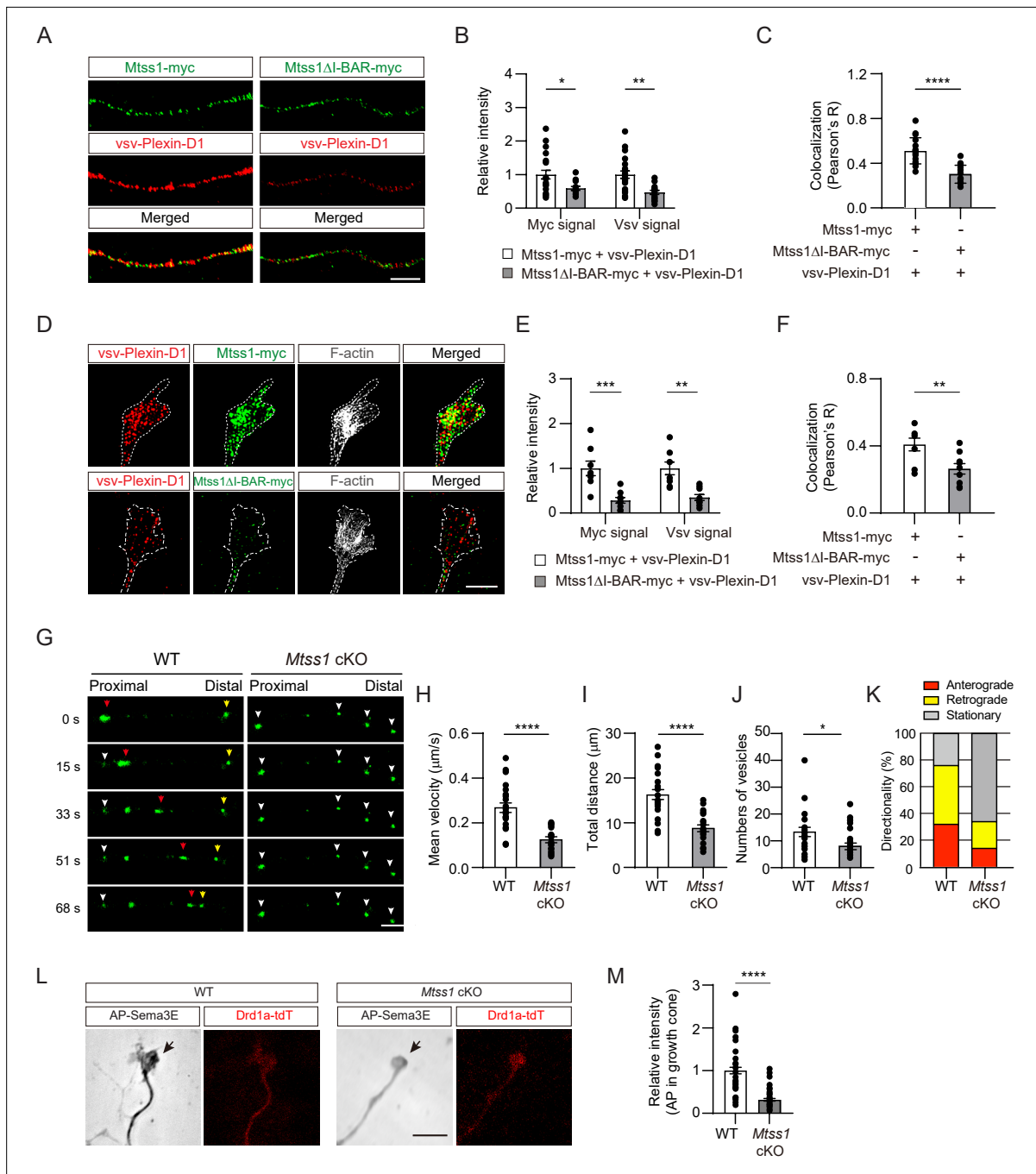


Figure 5. *Mtss1* facilitates Plexin-D1 transport to the growth cone in cultured *Drd1a*-positive medium spiny neurons (MSNs). **(A)** Immunocytochemistry for *Mtss1-myc* or *Mtss1ΔI-BAR-myc* (green), *vsv-Plexin-D1* (red) in the axons of MSNs transfected with *vsv-Plexin-D1* and *Mtss1-myc* or *Mtss1ΔI-BAR-myc*, using *Mtss1*-null mice as a background. The images were acquired using structured illumination microscopy (N-SIM). Scale bar, 5 μm .

(B) Quantification of the fluorescence intensity in the axons of **(A)**. Two-way ANOVA with Tukey's post hoc correction for multiple comparisons; *vsv-Plexin-D1*+*Mtss1-myc*, $n = 21$, and *vsv-Plexin-D1*+*Mtss1ΔI-BAR-myc*, $n = 14$. **(C)** Quantification of colocalization by Pearson's correlation coefficient calculated using Costes' randomized pixel scrambled image method. Student's *t*-test; *vsv-Plexin-D1*+*Mtss1-myc*, $n = 21$, and *vsv-Plexin-D1*+*Mtss1ΔI-BAR-myc*, $n = 14$. **(D)** Immunocytochemistry for *vsv-Plexin-D1* (red), *Mtss1-myc* (green), and F-actin (gray) in the growth cones of MSNs transfected with *vsv-Plexin-D1* and *Mtss1-myc* or *Mtss1ΔI-BAR-myc* originating from *Mtss1*-null mice. Scale bar, 5 μm . **(E)** Quantification of the intensities in the growth cones. The values represent the average fold change in expression compared to the control samples (*vsv-Plexin-D1*+*Mtss1-myc*). Two-way ANOVA with Tukey's post hoc correction for multiple comparisons; *vsv-Plexin-D1*+*Mtss1-myc*, $n = 8$, and *vsv-Plexin-D1*+*Mtss1ΔI-BAR-myc*, $n = 9$. **(F)** Quantification of colocalization by Pearson's correlation coefficient calculated using Costes' randomized pixel scrambled image method. Student's *t*-test; *vsv-Plexin-D1*+*Mtss1-myc*, $n = 8$, and *vsv-Plexin-D1*+*Mtss1ΔI-BAR-myc*, $n = 9$. **(G)** Representative time-lapse images of Plexin-D1-GFP-positive vesicles (green) from

Figure 5 continued on next page

Figure 5 continued

wild-type or *Mtss1* conditional knockout (cKO) MSNs at DIV6. Plexin-D1-positive vesicles transported toward distal or proximal directions are indicated by red and yellow arrowheads, respectively. White arrowheads indicate stationary vesicles. A mean velocity of less than 0.1 $\mu\text{m/s}$ was considered to be a stationary condition. See **Videos 1–4**. Scale bar, 5 μm . **(H–J)** Quantification of mean velocity (**H**), total travel distance (**I**), and number of vesicles (**J**) along neurites of Plexin-D1-positive vesicles. Student's t-test; $n = 23$ for WT, $n = 25$ for *Mtss1* cKO in four independent experiments. **(K)** Distribution analysis of vesicle directionality. **(L)** The AP-Sema3E binding assay was performed to visualize Plexin-D1 protein (black arrows) in the growth cones of WT or *Plxnd1*-deficient MSNs. Scale bar, 10 μm . **(L)** The AP-Sema3E binding assay performed to visualize Plexin-D1 protein (black arrows) in the growth cones of WT or *Mtss1*-deficient MSNs. Localization of Plexin-D1 (black arrows) in the growth cone investigated in cultured MSNs from WT (*Drd1a-tdT*; *Mtss1^{fl/fl}*) or *Mtss1* cKO (*Drd1a-tdT*; *Nes-cre*; *Mtss1^{fl/fl}*) mice. **(M)** Quantification of Plexin-D1 intensity shown in **(L)**. Mann-Whitney test; WT $n = 51$, KO $n = 50$. Error bars in all graphs, mean \pm SEM; * $p < 0.05$, ** $p < 0.01$, *** $p < 0.001$, **** $p < 0.0001$ by indicated statistical tests.

The online version of this article includes the following source data and figure supplement(s) for figure 5:

Figure supplement 1. *Mtss1* expression alters Plexin-D1 localization to the protrusion structure in COS7 cells without affecting its endocytosis or Sema3E binding.

Figure supplement 1—source data 1. Western blots shown in **Figure 5—figure supplement 1A and C**.

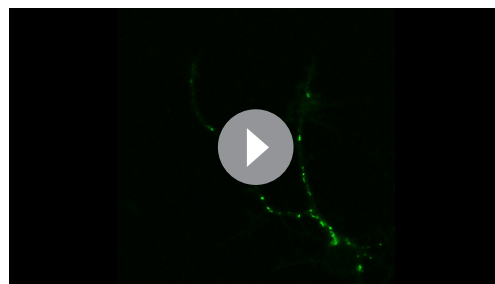
Figure supplement 2. No significant alteration in the expression of vsv-Plexin-D1 or *Mtss1*-myc or *Mtss1* Δ I-BAR-myc in the medium spiny neuron (MSN) soma.

directions in wild-type MSNs. In contrast, the Plexin-D1-positive vesicles in *Mtss1*-deficient MSNs remained stationary, and their overall numbers in neurites were also slightly reduced (**Figure 5G–K** and **Videos 1–4**). These observations demonstrate that *Mtss1* facilitates the dynamic transportation of Plexin-D1 along the growing neurites of direct-pathway MSNs, leading to an increased rate of Plexin-D1 localization in the growth cones.

Moreover, to examine whether endogenous *Mtss1* expression affects Plexin-D1 localization in the growth cone, leading to an active guidance role, we performed an AP-Sema3E binding analysis in *Drd1a*-positive MSNs at DIV6 (**Gu et al., 2005**). The AP-Sema3E binding assay has been used in many previous studies as an alternative method to detect endogenous Plexin-D1 protein due to the lack of reliable anti-Plexin-D1 antibodies (**Bellon et al., 2010**). The *Mtss1*-knockout neurons exhibited a low level of AP-Sema3E binding in the growth cones, indicating that the endogenous trafficking of Plexin-D1 to the tip of the growing axon is disrupted in the absence of *Mtss1* (**Figure 5L and M**). These results suggest that *Mtss1* serves to deliver Plexin-D1 to the growth cone.

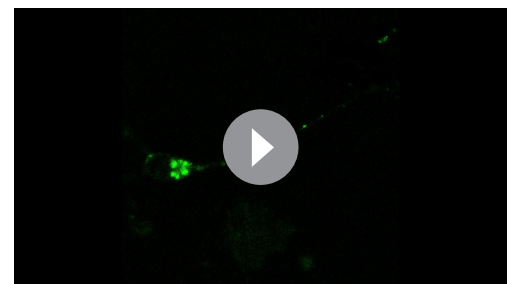
Plexin-D1 trafficking to the growth cone by *Mtss1* potentiates the repulsive response to Sema3E

Because *Mtss1* facilitates Plexin-D1 transport to the growth cone, proper Plexin-D1 localization at the membrane may contribute to the triggering of repulsive signaling by Plexin-D1 in response to Sema3E. To test this hypothesis, we performed a growth cone collapse assay at DIV3 in direct-pathway MSNs and found that wild-type *Drd1a*-tdT-positive striatal neurons underwent a high collapse rate after exogenous Sema3E treatment, whereas the growth cones of neurons lacking *Mtss1* did not collapse at a significantly different rate (**Figure 6A and B**). However, reintroduction of wild-type *Mtss1* into *Mtss1*-knockout MSNs resulted in growth cone collapse, but overexpressed *Mtss1* lacking the I-BAR domain



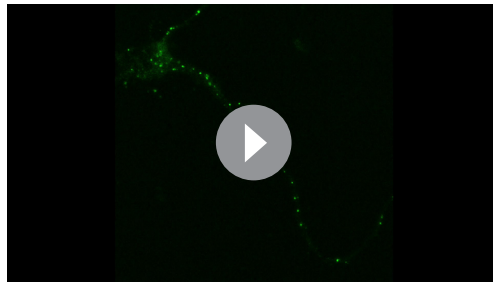
Video 1. Time-lapse live imaging of Plexin-D1-GFP-positive vesicles (green) from wild-type medium spiny neurons (MSNs) at DIV6_1.

<https://elifesciences.org/articles/96891/figures#video1>



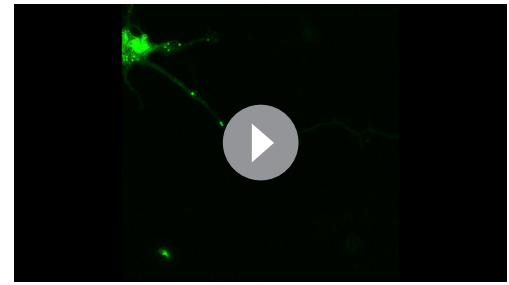
Video 2. Time-lapse live imaging of Plexin-D1-GFP-positive vesicles (green) from wild-type medium spiny neurons (MSNs) at DIV6_2.

<https://elifesciences.org/articles/96891/figures#video2>



Video 3. Time-lapse live imaging of Plexin-D1-GFP-positive vesicles (green) from *Mtss1* conditional knockout (cKO) medium spiny neurons (MSNs) at DIV6_1.

<https://elifesciences.org/articles/96891/figures#video3>



Video 4. Time-lapse live imaging of Plexin-D1-GFP-positive vesicles (green) from *Mtss1* conditional knockout (cKO) medium spiny neurons (MSNs) at DIV6_2.

<https://elifesciences.org/articles/96891/figures#video4>

showed less response to *Sema3E* (**Figure 6C and D**). In addition, *Plxnd1*-null MSNs also showed a very low collapse rate regardless of *Sema3E* addition at DIV6 (**Figure 6E**), consistent with a previous report that *Sema3E*-Plexin-D1 signaling acts as a repulsive guidance cue (**Chauvet et al., 2007**). The reduced collapse phenotypes were rescued by overexpression of full-length Plexin-D1 but not by ICD-deleted Plexin-D1 (**Figure 6F**). In summary, *Mtss1* targeting of Plexin-D1 to the growth cone is critical for robust *Sema3E*-induced repulsive signaling.

Absence of *Mtss1* reduces projection density and Plexin-D1 localization in the striatonigral pathway

First, to determine whether *Mtss1* is indeed expressed in the projecting striatonigral axons and their destination, the SNr, we performed immunostaining using wild-type or *Mtss1*-knockout mouse brains. We observed *Mtss1* localization in the striatonigral tract and SNr, but the immunostaining signal disappeared in *Mtss1*-deficient mice (**Figure 7—figure supplement 1**). Although we also detected *Mtss1* in the SNr region, we could not rule out the possibility that substantia nigra neurons express *Mtss1* at this stage. Next, to investigate the role of *Mtss1* in striatonigral pathway development *in vivo*, we performed an AP-*Sema3E* binding assay to examine the Plexin-D1-positive tract in brain tissue (**Chauvet et al., 2007**). In mice expressing wild-type *Mtss1*, a significant amount of Plexin-D1 was observed in the neuronal tract reaching the substantia nigra. In contrast, *Mtss1*-knockout mice exhibited a relatively small area of Plexin-D1-positive striatonigral tracts, including both poor neuronal projection and reduced Plexin-D1 localization at E17.5 (**Figure 7A–D**). In addition, despite these reduced neuronal projections in the *Mtss1*-knockout mice, the density of the AP-*Sema3E*-positive tracts was reduced even more (**Figure 7E**), indicating that the absence of *Mtss1* prevents both normal axonal projections and Plexin-D1 trafficking. In the coronal view, the bundle density of Plexin-D1-positive projections passing between the rTh and Gp was reduced in the *Mtss1*-knockout mice (**Figure 7F**). Because most mice with conditional Nestin-Cre-driven *Mtss1* deletion were born alive, we analyzed the Plexin-D1-positive striatonigral pathway at P5. Consistent with the results obtained with E17.5 embryos, *Mtss1*-deficient neonates showed fewer Plexin-D1-positive striatonigral projections in the coverage area and a reduced path width (**Figure 7G–J**).

To further identify Plexin-D1-positive striatonigral pathway defects, we crossed *Drd1a*-tdT transgenic reporter mice with conditional *Mtss1*-knockout mice and visualized the pathway in the offspring. Consistent with the results shown in AP-*Sema3E* binding experiments, the total boundary area with *Drd1a*-tdT-positive projections was smaller and less compact in the *Mtss1*-knockout mice than in the wild-type mice at P5 (**Figure 7K–M**). At P30, the projection density defects were more obvious, but the boundary area in the wild-type and mutant mice was not significantly different, indicating that *Mtss1* deficiency led to the formation of fewer striatonigral axonal bundles (**Figure 7—figure supplement 2A–C**). We assumed that *Mtss1* regulates the initial striatonigral axonal projection during development of the neonate and that the pathway establishment ends by P7 (**Morello et al., 2015**) therefore, the scarcity of the projections may be clearer when the brain increases to the adult size. Moreover, we examined whether *Mtss1* expression affects Plexin-D1 levels on the *Drd1a*-tdT-positive tracks at P5 using the same methodology as employed at E17.5 (**Figure 7A**). Our findings revealed a decreased

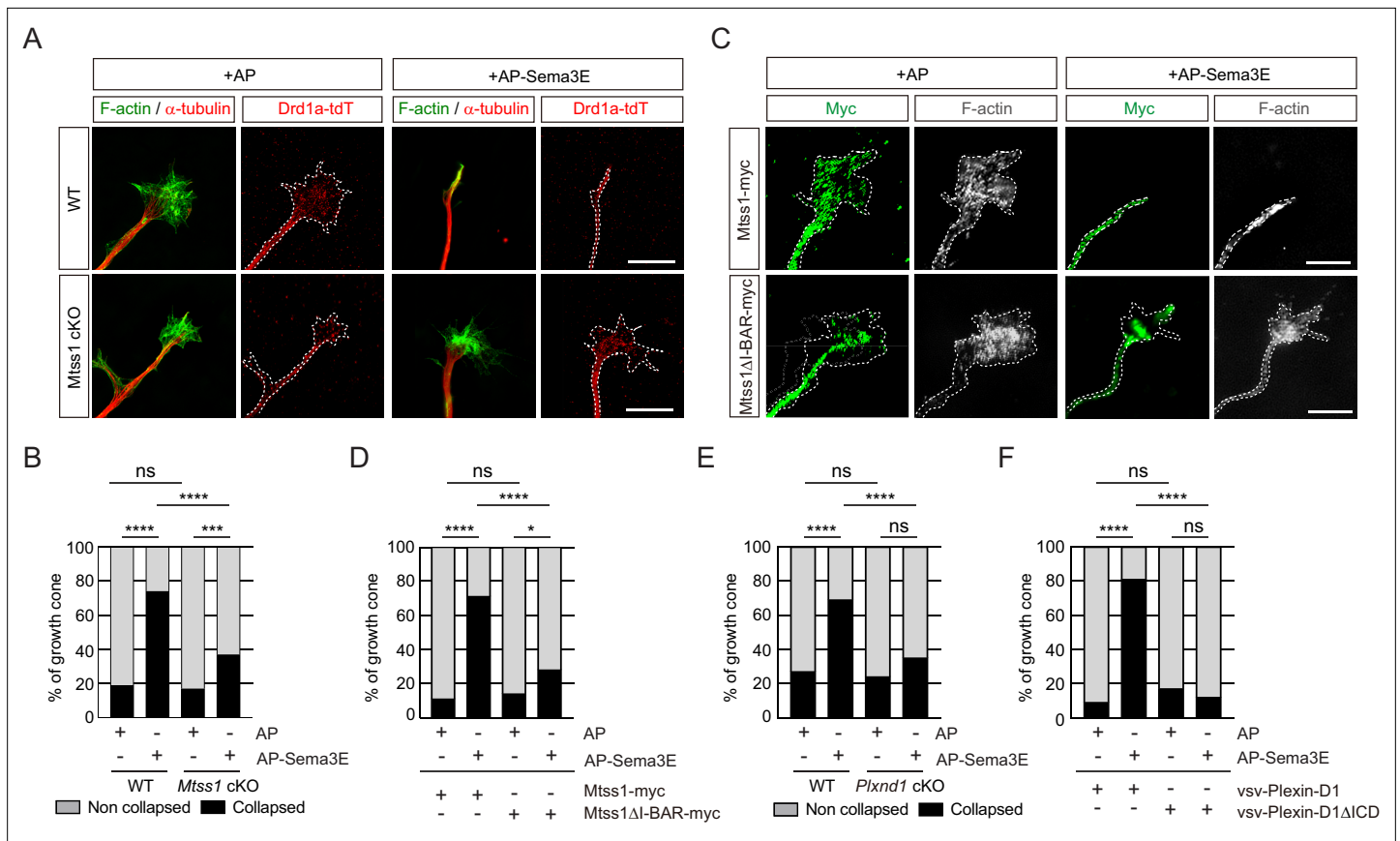


Figure 6. The repulsive response through Sema3E-Plexin-D1 signaling is attenuated in the absence of *Mtss1*. **(A)** A growth cone collapse assay in the presence or absence of Sema3E (2 nM) was performed with medium spiny neuron (MSN) cultures derived from wild-type (WT) (*Drd1a-tdT*; *Mtss1^{fl/fl}*) or *Mtss1*-KO (*Drd1a-tdT*; *Nes-cre*; *Mtss1^{fl/fl}*) mice at DIV3. Scale bar, 10 μ m. The images were obtained from structured illumination microscopy (N-SIM). **(B)** Quantification of collapsed growth cones in **(A)**. Error bars, mean \pm SEM; *** p <0.001, **** p <0.0001 by χ^2 test; WT + AP, n = 155, WT + AP-Sema3E, n = 163, KO + AP, n = 149, KO + AP-Sema3E, n = 149. **(C)** A growth cone collapse assay in the presence or absence of Sema3E (2 nM) was performed with MSN cultures following ectopic expression of *Mtss1*-myc or *Mtss1* Δ I – B A R-myc in the *Mtss1*-null background at DIV3. Scale bar, 10 μ m. **(D)** Quantification of collapsed growth cones in **(C)**. Error bars, mean \pm SEM; *** p <0.001, **** p <0.0001 by χ^2 test; *Mtss1*-myc+AP, n = 28, *Mtss1* Δ I-BAR-myc+AP-Sema3E, n = 28, *Mtss1* Δ I – B A R-myc+AP-Sema3E, n = 43. **(E)** Quantification of the collapse assay in the presence or absence of Sema3E (2 nM) was performed with MSN cultures at DIV6 from WT (*Drd1a-tdT*; *Plxnd1^{fl/fl}*) or *Plxnd1*-KO (*Drd1a-tdT*; *Nes-cre*; *Plxnd1^{fl/fl}*) mice. **** p <0.0001 by χ^2 test; WT + AP, n = 44, WT + AP-Sema3E, n = 45, KO + AP, n = 45, KO + AP-Sema3E, n = 46. in three independent experiments. **(F)** Quantification of a growth cone collapse assay in the presence or absence of Sema3E (2 nM) was performed with MSN cultures following ectopic expression of vsv-Plexin-D1 or vsv-Plexin-D1 Δ ICD in the *Plxnd1*-KO background at DIV6. **** p <0.0001 by χ^2 test; vsv-Plexin-D1+AP, n = 35, vsv-Plexin-D1+AP-Sema3E, n = 32, vsv-Plexin-D1 Δ ICD + AP, n = 30, vsv-Plexin-D1 Δ ICD + AP-Sema3E, n = 26 in three independent experiments. tdT, tdTomato.

ratio of AP-Sema3E binding per tdT staining, suggesting that *Mtss1* is implicated not only in axonal projections but also in Plexin-D1 trafficking in navigating striatonigral projections (**Figure 7N–Q**).

We then investigated whether *Mtss1* specifically contributes to the development of descending striatonigral projections rather than dendritic arborization. Since global *Mtss1*-mutant mice have enlarged brain ventricles and decreased cortical thickness (*Minkeviciene et al., 2019*), we first examined whether the axonal projection in *Mtss1*-knockout mice is due to cellular death of MSNs in the striatum. Using cleaved caspase 3 staining to detect apoptotic cells, we found few dying cells in the wild-type and *Mtss1*-mutant neonates (**Figure 7—figure supplement 3A and B**), indicating that no significant cell pathology was induced by *Mtss1* expression deficiency. Because *Mtss1* is selectively expressed in direct-pathway MSNs, which comprise approximately 45% of striatal neurons (**Figure 1**), we expected that Golgi staining would be sufficient to detect any dendritic defects, such as aberrant number and/or length of branches. However, we found no detectable difference between the wild-type and *Mtss1* mutants at P5 (**Figure 7—figure supplement 3C–E**). In addition, no significant

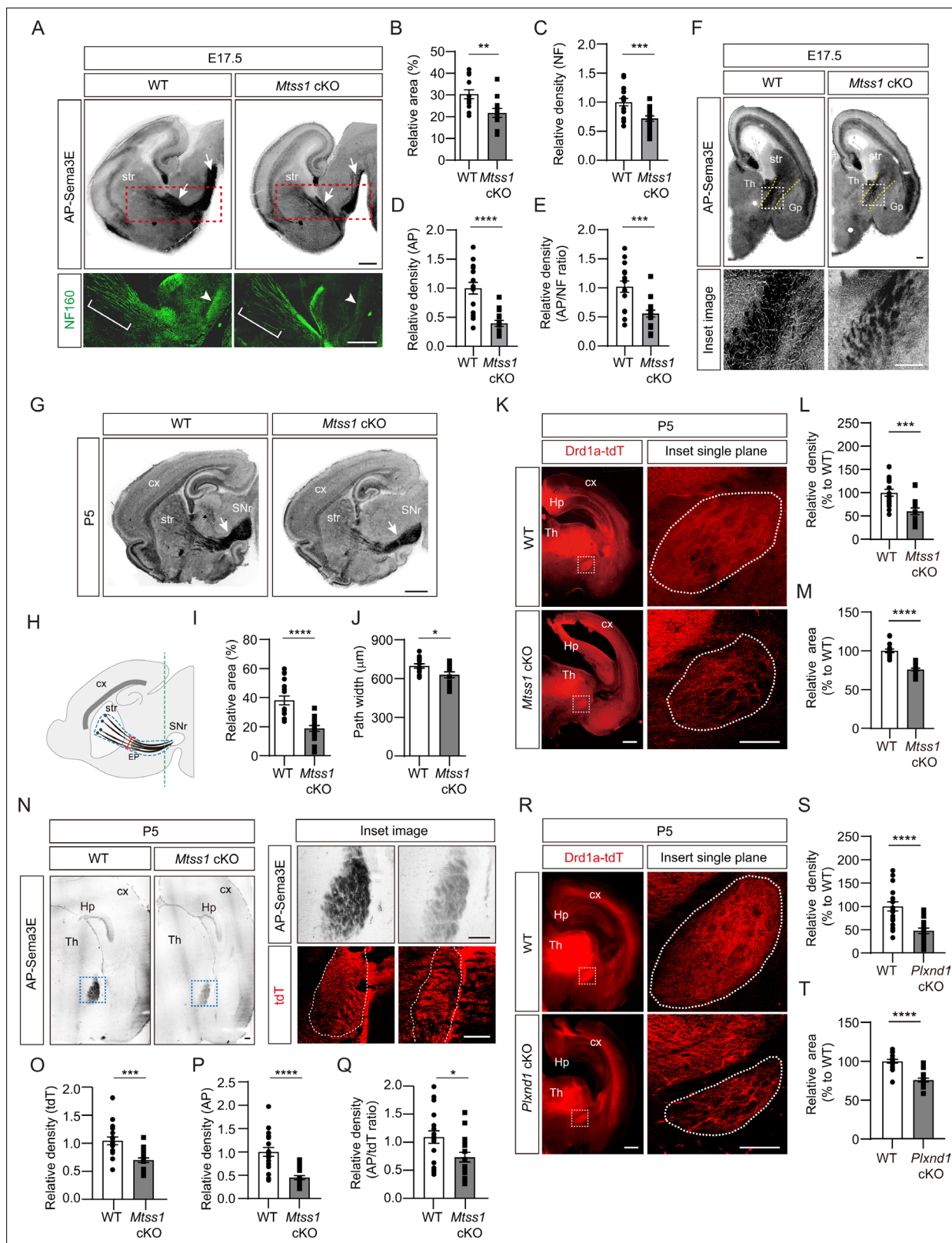


Figure 7. A reduced number of Plexin-D1 molecules localize to the developing striatonigral projections in *Mtss1*-deficient mice. **(A)** AP-Sema3E binding assay (top) to detect Plexin-D1 expression (white arrows) in striatonigral projections and immunohistochemistry (bottom) for neurofilaments (NFs) indicated by red dotted square, performed in adjacent parasagittal sections at E17.5 of wild-type (WT) or *Mtss1* conditional knockout (cKO) mice. The diminished projections are marked by white brackets (middle of the striatum) and arrowheads (near substantia nigra regions). Scale bar,

Figure 7 continued on next page

Figure 7 continued

500 μm . (B) Quantification of the Plexin-D1-positive area in the total striatonigral projection at E17.5 of WT or *Mtss1* cKO mice. Student's *t*-test; WT, $n = 12$, KO, $n = 12$ (three sections/mouse). (C) Quantification of the fluorescence density (intensity/area) of NF in striatonigral projections at E17.5 in WT or *Mtss1* cKO mice. Student's *t*-test; WT, $n = 16$, KO, $n = 17$ (three or four sections/mouse). (D) Quantification of the AP density (intensity/area) in striatonigral projections at E17.5 in WT or *Mtss1* cKO mice. Student's *t*-test; WT, $n = 16$, KO, $n = 17$ (three or four sections/mouse). (E) The ratio of AP to NF density (intensity/area). Student's *t*-test; WT, $n = 16$, KO, $n = 17$ (three or four sections/mouse). (F) Coronal view of Plexin-D1 localization in striatonigral projections at E17.5 in WT or *Mtss1* cKO mice. Yellow dotted lines indicate the corridor between the thalamus and globus pallidus. Insets show the images in dotted boxes at higher resolution. Scale bar, 200 μm . (G) Representative images of Plexin-D1 molecules in striatonigral projections visualized by AP-Sema3E binding assay in WT or *Mtss1* cKO mice at P5. White arrows indicate striatonigral projections. Scale bar, 1 mm. (H) Schematic representing the quantified region. The dotted blue lines indicate the striatonigral projection-covering areas. The width (red segment) of the striatonigral tract was measured as previously described (Burk et al., 2017). (I, J) Quantification of the Plexin-D1-positive area (%) in dotted blue area and projection width at P5 according to the scheme shown in (H). Mann-Whitney test (I) and Student's *t*-test (J). $n = 18$ (three sections/mouse). (K) Immunohistochemistry of coronal sections of striatal projections labeled with td-Tomato endogenously expressed through the *Drd1a* promoter in WT (*Drd1a-tdT*; *Mtss1^{fl/fl}*) or *Mtss1* cKO mice (*Drd1a-tdT*; *Nes-cre*; *Mtss1^{fl/fl}*) at P5. The white dotted boxes on the left images are shown in the inset images on the right, which were captured in a single plane using a high-resolution confocal microscope. Scale bar, 500 μm . (L, M) Quantification of the density (intensity/area) (L) and area size (M) of the striatonigral projection in the dotted region in the inset images. Mann-Whitney test (L) and Student's *t*-test (M); $n = 18$ per group (six sections/mouse). (N) AP-Sema3E binding assay and tdT immunostaining in adjacent sections of WT or *Mtss1* cKO mice located near the SNr. The green line in (H) indicates the location for cross-sectioning. The inset images of Plexin-D1-positive striatonigral projections were taken from the blue dotted boxes on the left panels. The dotted white lines indicate the tdT-positive striatonigral projections. Scale bar, 200 μm . (O, P) Quantification of the density (intensity/area) of tdT (O) and AP (P) of striatonigral projections WT or *Mtss1* cKO mice. (Q) The ratio of AP to tdT density (intensity/area). Student's *t*-test; WT, $n = 18$, KO, $n = 18$ (six sections/mouse). (R) Immunohistochemistry of coronal views of striatonigral projections in WT (*Drd1a-tdT*; *Plxnd1^{fl/fl}*) or *Plxnd1* cKO mice (*Drd1a-tdT*; *Nes-cre*; *Plxnd1^{fl/fl}*) at P5. The white dotted boxes on the left images are shown in the inset images on the right, which were obtained using a high-resolution confocal microscope in a single plane. Scale bar, 500 μm . (S, T) Quantification of the density (intensity/area) of tdT (S) and area size (T). Student's *t*-test; $n = 18$ per group (six sections/mouse). Error bars, mean \pm SEM; * $p < 0.05$, ** $p < 0.01$, *** $p < 0.001$, **** $p < 0.0001$ by indicated statistical tests. str, striatum; cx, cortex; Th, thalamus; SNr, substantia nigra; EP, entopeduncular nucleus; Gp, globus pallidus; Hp, hippocampus.

The online version of this article includes the following source data and figure supplement(s) for figure 7:

Figure supplement 1. Expression of *Mtss1* in the striatonigral tract and SNr at P5.

Figure supplement 2. *Mtss1* or Plexin-D1 deficiency reduced striatonigral axonal bundles without altering striatonigral projection patterns at P30.

Figure supplement 3. The absence of *Mtss1* does not affect medium spiny neuron (MSN) survival, dendritic arborization, and Plexin-D1 expression during striatonigral pathway development.

Figure supplement 3—source data 1. Raw uncropped western blot & gel images.

Figure supplement 4. Striatonigral projection defects are observed in *Sema3e*-null mice at P5.

change in Plexin-D1 levels was observed in the striatum or cultured neurons of *Mtss1*-deficient mice compared to those in littermate controls (Figure 7—figure supplement 3F–I). These results indicate that the weakening of the Plexin-D1-positive striatonigral pathway in *Mtss1*-knockout mice is caused by both impairments of neuronal projections and inappropriate Plexin-D1 distribution due to *Mtss1* downregulation.

The absence of Plexin-D1 or Sema3E reduces the axonal projection of direct-pathway MSNs

Since *Mtss1* expression is under the control of Sema3E-Plexin-D1 signaling, we investigated whether *Plxnd1* deletion leads to phenocopying of the striatonigral projection defects observed in *Mtss1*-knockout mice. During the neonatal period, the boundary area and compactness of descending striatonigral projections were small and loose in the *Plxnd1*-knockout mice, but only a reduced projection density was observed in adult mice, which was similar to that of *Mtss1*-knockout mice (Figure 7R–T, Figure 7—figure supplement 2D–F). Moreover, *Sema3e*-knockout at P5 also showed these projection defects, albeit somewhat milder compared to those observed in *Plxnd1*- or *Mtss1*-deficient mice (Figure 7—figure supplement 4A–E). These phenocopy results suggest that activation of Sema3E-Plexin-D1 signaling, which leads to induction of *Mtss1*, is required for the striatonigral trajectory during the axonal pathfinding period.

Absence of *Mtss1* or Plexin-D1 results in irregular projection patterns in direct-pathway MSNs

Subsequently, we examined whether striatonigral projection patterns are altered by *Mtss1* deficiency. Interestingly, we observed that the descending striatonigral projections in the wild-type mice were relatively straight and untangled near the Gp region through the sagittal view (**Figure 8A**). When visualizing the striatonigral projection using 3D imaging by sparsely labeling with Dil injection at the dorsal striatum, the axonal bundles appeared relatively fasciculated and straight in the wild-type at P5 (**Figure 8B and C**). However, *Mtss1* mutants showed irregular projection patterns with random directionality and mild defasciculation (**Figure 8A–C**). To assess axonal deviation, we measured the number of projections intersecting each other in the same region, as shown in **Figure 8A and B**. The deficiency of *Mtss1* led to more deviant ectopic projections (**Figure 8E**). However, the misguidance defects were not apparent at P30, likely because abnormal projections were discarded as mice matured into adults (**Figure 7—figure supplement 2G**). These results suggest that inefficient Plexin-D1 trafficking to the extending axons in the *Mtss1*-knockout mice may have weakened the proper guidance response.

Previous studies have reported that *Sema3E*-Plexin-D1 signaling defects lead to ectopic projection during development or misguidance in the adult striatonigral pathway (**Chauvet et al., 2007; Ehrman et al., 2013**), but these phenotypes were not detected in our study. Instead, we also observed irregular projection patterns near the Gp in *Plxnd1*-knockout mice at P5 but not at P30 (**Figure 8D and F, Figure 7—figure supplement 2H**), similar to those seen in *Mtss1*-knockout mice. Moreover, *Sema3E*-knockout at P5 showed a few axonal bundles deviated from their typical trajectories (**Figure 7—figure supplement 4F and G**). These results demonstrate that *Sema3E*-Plexin-D1 signaling, probably in concert with *Mtss1* molecules, is specifically involved in the proper guidance of descending striatonigral projections. Collectively, our results confirm that *Sema3E*-Plexin-D1 signaling activates *Mtss1* action, through which striatonigral neurons are extended and steered through the proper route to the target destination (**Figure 8J**).

Finally, since *Sema3E*-Plexin-D1 is well known to regulate both neural and vascular development (**Oh and Gu, 2013a**), we wondered whether *Mtss1* also plays a role in the vasculature as a downstream player of the common guidance cue. Although it was expressed in neuronal cells, *Mtss1* was not detected in vascular endothelial cells expressing Plexin-D1 during development (**Figure 8—figure supplement 1A**). In addition, *Mtss1*-knockout mice did not result in an obvious intersomatic vasculature defect, which is a typical phenotype observed in *Sema3E* or *Plxnd1* mutants (**Burk et al., 2017; Gu et al., 2005; Figure 8—figure supplement 1B**). Interestingly, *Mtss1* was highly expressed in the two different types of cultured endothelial cells but was not controlled by *Sema3E*-Plexin-D1 signaling (**Figure 8—figure supplement 1C**). These results provide evidence that the activation of *Mtss1* by the *Sema3E*-Plexin-D1 signaling pathway and its function in neurons could be selective and distinct.

Discussion

There are two main aspects of the traditional axon guidance concept: attractive cue-guided axon growth and repulsive cue-guided axon growth. In these processes, the axon terminals are constantly facing both types of signals en route to their destination. In the present study, we show that repulsive guidance cues, namely, *Sema3E*-Plexin-D1 pairs, induce a dual-functioning facilitator, *Mtss1*, through which navigating axons ensure incessant extension to their target tissues while exhibiting sensitivity and subsequent steering in response to repulsive signals. In our model (**Figure 8—figure supplement 2**), Plexin-D1 on the cell body of direct-pathway MSNs in the striatum receives its specific ligand, *Sema3E*, through the thalamostriatal projection at the late embryonic stage and induces a unique pool of regulatory factors, including *Mtss1*. *Mtss1* then generates axonal projections to targets in the substantia nigra while enabling Plexin-D1 to transport along axons. In the growth cones, *Mtss1* promotes membrane curvature to form a protruding filopodium, and Plexin-D1 is positioned on the cell surface to sense the external repulsive guidance signals from *Sema3E*. Currently, it is not clear whether Plexin-D1 and *Mtss1* are present as a complex at the membrane surface of the growth cone, but *Mtss1* does not seem to directly affect the repulsive signaling activation of *Sema3E*-Plexin-D1. In this way, *Mtss1* provides an efficient transport system for its own activator during striatonigral axon growth and potentiates the repulsive guidance cue.

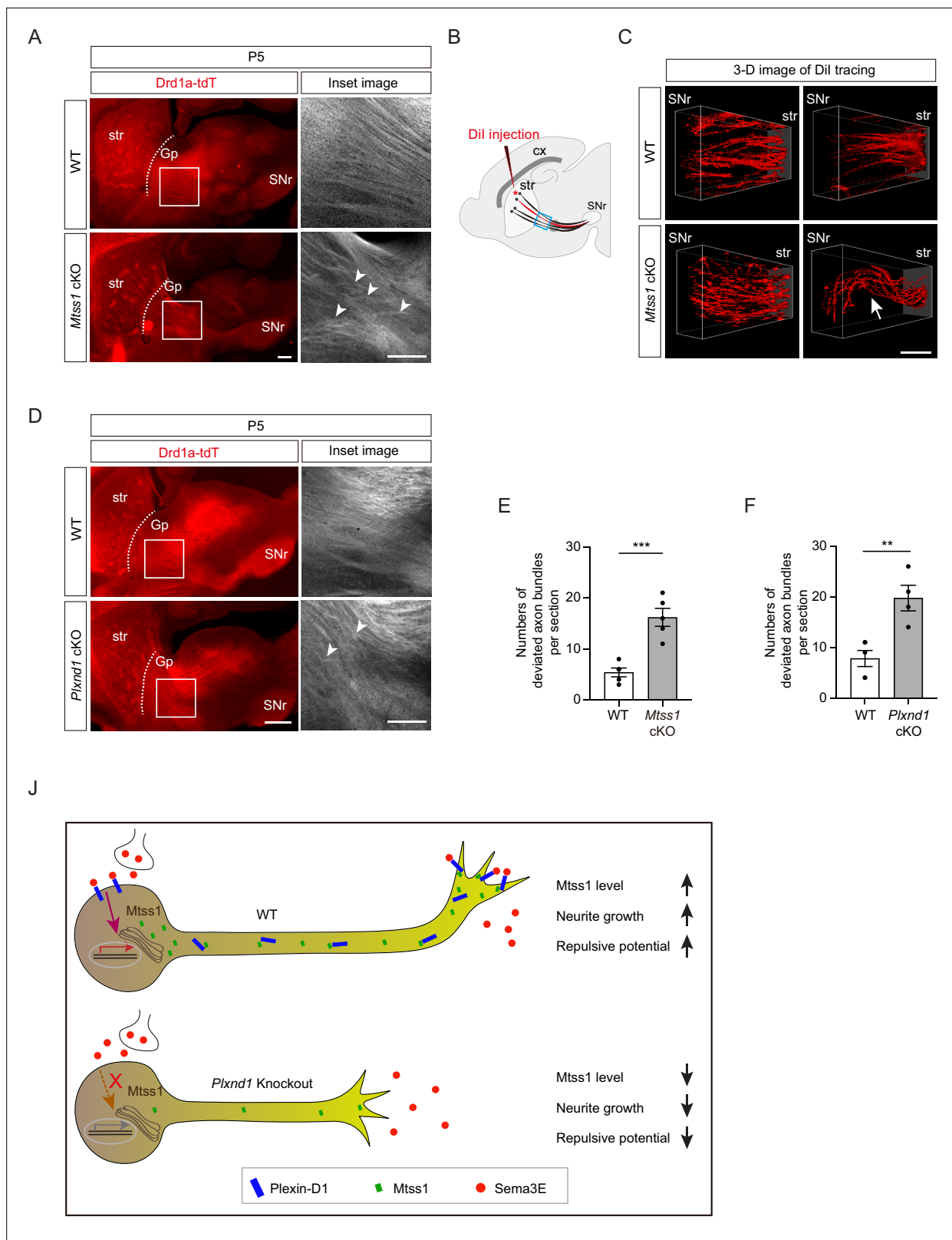


Figure 8. Direct-pathway medium spiny neurons (MSNs) exhibit irregular projection patterns in the absence of either Mtss1 or Plexin-D1. **(A)** Immunohistochemistry of parasagittal sections of striatonigral projections labeled with Drd1a-tdT in wild-type (WT) or Mtss1 conditional knockout (cKO) mice at P5. The white boxes on the left images are shown in the inset image on the right. Misguided striatonigral projections are indicated by white arrowheads. The phenotype was observed in five out of five Mtss1 cKO mice at P5. Scale bar, 500 μ m. **(B)** Schematics depicting Dil injection (red) *Figure 8 continued on next page*

Figure 8 continued

asterisk) into the dorsal striatum for sparse labeling of striatonigral projections. The regions indicated in the blue square were captured for three-dimensional (3D) visualization. (C) Representative 3D images of Dil-labeled axonal tracks in WT or *Mtss1* cKO mice at P5. Compared to the fasciculated straight projections in WT (top panels), the striatonigral projections of *Mtss1* cKO mice presented relatively defasciculated (bottom panels) and occasionally severely misrouted patterns (white arrow in the bottom-right panel). The phenotype was observed in three out of three *Mtss1* cKO mice. Scale bar, 200 μm . (D) Representative images showing parasagittal sections of brains from WT or *Plxnd1* cKO mice at P5. The misrouted projections are also indicated by white arrowheads in the magnified inset images. The phenotype was observed in four out of four *Plxnd1* cKO mice at P5. Scale bar, 500 μm . (E, F) Quantification of the number of intersecting axonal bundles within the corresponding area from *Mtss1* cKO (A) or *Plxnd1* cKO (D). (E) Student's *t*-test; $n = 5$ mice for WT, $n = 5$ mice for *Mtss1* cKO. (F) Student's *t*-test; $n = 5$ mice for WT, $n = 4$ mice for *Plxnd1* cKO. Error bars, mean \pm SEM; ** $p < 0.01$, *** $p < 0.001$ by indicated statistical tests. (J) Model showing that *Mtss1*, upregulated by the *Sema3E*-*Plexin-D1* signaling pathway, promotes axonal growth and directs *Plexin-D1* to the growth cone to receive a repulsive guidance signal.

The online version of this article includes the following source data and figure supplement(s) for figure 8:

Figure supplement 1. No *Mtss1* was found in endothelial cells at E14.5, and no vascular defects were observed in *Mtss1*-conditional knockout (KO) mice.

Figure supplement 1—source data 1. Western blots shown in **Figure 8—figure supplement 1C**.

Figure supplement 2. Schematic summary showing striatonigral projection development via a serial reciprocal interaction of the *Sema3E*-*Plexin-D1*-*Mtss1* complex.

Gene expression by axon guidance signaling

Although many studies have reported the identification of proteins locally synthesized in the axon terminal (Jung et al., 2012), most proteins required for growth cone behavior are generated in and delivered from the soma. Because of the diverse roles of guidance molecules, such as driving neuronal cell migration, cell death, and axonal regeneration, as well as in traditional axonal navigation in the nervous system (Kolodkin and Tessier-Lavigne, 2011), guidance signaling is generally thought to be involved in the activation of a gene expression program in the nucleus. However, few studies have examined gene expression changes induced by guidance signaling at the level of transcriptional regulation, and the most definitive results have been obtained in the *Drosophila* model (Russell and Bashaw, 2018). A well-described example is the Frazzled (Fra) receptor in the regulation of midline axon crossing in *Drosophila*, where the truncated ICD of Fra is generated by gamma-secretase and enters the nucleus to activate transcription of the *commis sureless* (*comm*) gene (Neuhaus-Follini and Bashaw, 2015). In a rodent model, microarray analysis of the Robo mutant revealed hundreds of DEGs that may be related to the dynamics of neuronal progenitors in the developing cortex (Yeh et al., 2014). Another example is Eph-Ephrin signaling in neural progenitor cells, where Ephrin-B1 reverse signaling downregulates miR-124 expression to inhibit neurogenesis as a posttranscriptional repressor (Arvanitis et al., 2010).

Through a bulk RNA-seq analysis, we showed that *Sema3E*-*Plexin-D1* signaling changed the expression of specific genes, including *Mtss1*, required for the precise axon guidance of striatonigral neurons. Since ablation of *Plexin-D1* expression results in the ectopic formation of thalamostriatal synapses on the MSN cell body as well as on dendrites (Ding et al., 2012), it is likely that *Plexin-D1* is expressed in the soma of MSNs and is capable of transmitting gene expression signals. Although *Sema3E*-*Plexin-D1* signaling regulated the expression of a set of genes in the present study, the precise signaling cascade that extends into the nucleus is still not completely understood. Nevertheless, we cannot dismiss the possibility that *Mtss1* expression activation through *Sema3E*-*Plexin-D1* signaling may be subject to post-transcriptional or translational regulatory mechanisms. Thus, to uncover the molecular mechanism through which these guidance molecules mediate specific gene expression or ensure stability, comprehensive studies on gene regulation in a suitable homogeneous cellular model are necessary. A growing body of evidence demonstrates that diverse extracellular stimuli induce mechanotransduction through dynamic changes in the actin and microtubule cytoskeletal networks, which depend on Rho family proteins to cascade signals in the cytosol and nucleus to activate gene expression (Dupont and Wickström, 2022; Giehl et al., 2015; Miralles et al., 2003; Percipalle and Visa, 2006; Samarakoon et al., 2010). Previously, *Sema3E*-*Plexin-D1* signaling was shown to modulate such cytoskeletal rearrangement through the PI3K/Akt pathway in regulating endothelial cell mobility, axonal growth, and growth cone collapse (Aghajanian et al., 2014; Bellon et al., 2010; Burk et al., 2017). Likewise, we found that disturbance of Akt signaling reduced *Mtss1* expression in young

cultured MSNs, suggesting that activation of *Sema3E*-Plexin-D1 signaling induces specific molecule expression through similar Akt-mediated actin dynamics.

Despite the fact that *Mtss1* is a downstream molecule under *Sema3E*-Plexin-D1 signaling, it is still puzzling how *Mtss1* expression is specifically and selectively regulated during striatonigral pathfinding. Since *Mtss1* expression did not appear to be affected by *Plxnd1*-knockout at early embryonic stages and some level of *Mtss1* persisted in cultured neurons lacking *Sema3e* or *Plxnd1*, we cannot exclude the possibility that other pathways activate *Mtss1* expression. Nevertheless, it is certain that *Mtss1* expression is under *Sema3E*-Plexin-D1 signaling activation during striatonigral projection and that, when axons reach their destination at P7, *Mtss1* expression is downregulated. Such concurrence of *Mtss1* downregulation and axonal projection leads us to speculate that target-derived factor-driven retrograde signaling may be involved in this gene regulation (Harrington and Ginty, 2013), and elucidating the relevant mechanism may be an interesting objective for future study. Furthermore, it is noteworthy that levels of both Plexin-D1 and *Mtss1* were exclusively upregulated during the late gestation to early postnatal period, followed by an abrupt downregulation. Therefore, it is plausible that the activation of *Mtss1* relies on the reinforcement of Plexin-D1 signaling. During angiogenic sprouting, the expression of Plexin-D1 in endothelial cells is controlled by VEGF signaling (Kim et al., 2022; Yu et al., 2022). However, the upstream pathway responsible for Plexin-D1 expression in neurons and the precise regulation of signaling strength in this context is still uncertain.

Trafficking of Plexin-D1-Mtss1 in striatonigral neurons

Another intriguing finding in our study is that Plexin-D1-containing vesicles undergo both anterograde and retrograde movement along neurites in cultured direct-pathway MSNs. Until now, neurotrophin or semaphorin 3A-mediated retrograde trafficking has been extensively studied due to its crucial role in controlling the growth of axons and dendrites, promoting neuronal survival, and facilitating synaptogenesis within the peripheral nervous system. Additionally, finely regulated anterograde transport is essential for replenishing receptors on the growth cone surface to ensure the responses of appropriate target-derived guidance signals (Scott-Solomon and Kuruvilla, 2018; Yamashita, 2019). We observed that *Mtss1* contributes to the Plexin-D1 localization in the growth cone of cultured MSNs and in the terminal region of descending striatonigral projections. Previously, it has been reported that signaling endosomes containing *Sema3A*/Plexin-A at the axonal growth cones are retrogradely transported to soma. This process facilitates the localization of AMPA receptor GluA2 to the distal dendrites, thereby regulating dendritic development in the cultured hippocampal neurons (Yamashita et al., 2014). Since it is known that Plexin-D1 plays a role in the somatodendritic synaptogenesis of direct-pathway MSNs (Ding et al., 2012), the connection of the retrograde trafficking Plexin-D1-positive vesicles in this process or other developmental mechanisms like retrograde *Sema3A* signaling in the soma remains to be elucidated.

Axon-specific role of *Sema3E*-Plexin-D1-Mtss1 in striatonigral neuron

Sema3E-Plexin-D1 signaling is involved in dendritic synapse formation during the postnatal stage as well as traditional axon projection from the embryonic to the postnatal stage in the basal ganglia circuit (Ding et al., 2012). In addition, since axon projection and synapse formation are sequential events that occur in different cellular compartments during circuit establishment (Kuo and Liu, 2019), *Sema3E*-Plexin-D1 signaling may play discrete roles within different parts of a neuron, such as the dendrite versus the axon, through a unique subset of molecules. Indeed, our observations that the duration of *Mtss1* expression coincided with active striatonigral axon pathfinding, *Mtss1* was significantly expressed on the axonal side, and axon projection defects were observed after *Sema3E*-Plexin-D1 signaling disruption suggest that the *Sema3E*-Plexin-D1-Mtss1 complex appears to mainly regulate axon projection and guidance, at least during striatonigral pathway development. However, the cellular distribution of *Mtss1* is somewhat controversial, as its expression is mainly observed on the dendritic side of Purkinje cells and hippocampal neurons, and its knockout shows defective dendritic arborization and spine formation (Kawabata Galbraith et al., 2018; Saarikangas et al., 2015; Yu et al., 2016), while a study has also shown that *Mtss1* is more localized in the axoplasmic compartment of Purkinje cells (Hayn-Leichsenring et al., 2011). In this study, *Mtss1*-knockout did not show clear dendritic changes in MSNs, at least at P5 when an active axon trajectory occurs; however, given the enlarged ventricle and decreased cortical volume phenotype in knockout adults (Minkeviciene

et al., 2019), later *Mtss1* expression (even at low levels) may affect overall dendritic development. Consistent with this assumption, a previous study reported a slight decrease in dendritic spine density but a slight increase in the number of dendritic crossings without a change in total dendritic length in the direct pathway MSNs of 3- to 4-week-old *Plxnd1*- or *Sema3e*-knockout mice (*Ding et al., 2012*). Thus, we cannot exclude the possibility that the *Sema3E*-Plexin-D1-*Mtss1* complex modulates MSN dendritic development later than the axonal pathfinding period.

Counterintuitive mechanism of attractive and repulsive guidance by *Mtss1*

From a traditional guidance point of view, our finding was somewhat unexpected because it was counterintuitive: conventional repulsive guidance cues that mediate growth inhibition induce upregulation of a positive regulator of neurite extension. We revealed that *Mtss1* plays a dual role in striatonigral neurons, axon extension by membrane protrusion ability, and axon guidance by efficient Plexin-D1 trafficking to the growth cone. Therefore, our findings represent two important discoveries regarding the axon guidance mechanism. First, axon guidance signaling can switch on the specific regulatory program necessary for facilitating its own function, thereby generating the appropriate machinery to accomplish an intrinsic guidance role during neuronal pathfinding. Second, molecules such as *Mtss1* coordinate positive and negative growth potentials in the axonal pathfinding route. Axon guidance cues require various auxiliary proteins to perform their programmed functions, in particular, transporting guidance receptors to the growth cone, endocytic sorting, and activating signaling cascades (*O'Donnell et al., 2009*), but none of the cofactors discovered to date have induced direct expression regulation of the guidance signaling with which it is involved. Previous studies have shown that *Sema3E*-Plexin-D1 signaling can switch its role from repulsive to attractive by interacting with the coreceptors neuropilin-1 (*Npn1*) and vascular endothelial growth factor receptor type 2 (*VEGFR2*) in subiculum neurons (*Bellon et al., 2010; Chauvet et al., 2007*). This mechanism is not applicable to developing striatonigral MSNs because the *Npn1* receptor is not expressed in early postnatal striatal neurons (*Ding et al., 2012*). Instead, striatonigral neurons seem to adopt a new strategy, such as activating their own attractive driver to promote axonal growth. From a phenotypic perspective, it is also plausible that the positive or negative guidance roles of *Mtss1* may be interdependent. Striatonigral extension defects could potentially lead to inadequate responses to *Sema3E* signals during pathfinding, consequently resulting in misguided projections. Similarly, guidance defects may disrupt normal signaling processes within the growth cone, thereby transmitting incorrect information for the replenishment of Plexin-D1 to the soma. This erroneous signaling could weaken *Mtss1* expression and normal trafficking, ultimately leading to axonal growth defects.

Diverse roles of BAR domain proteins in the axon guidance signaling pathway

Mtss1 promotes membrane curvature through the I-BAR domain and induces the redistribution of lipids in the membrane, thereby increasing the local phosphatidylinositol 4,5-bisphosphate (PIP_2) level at the negatively curved membrane. The elevation of local PIP_2 levels leads to membrane binding of the I-BAR domain via electrostatic interactions (*Lin et al., 2018*). Interestingly, *Sema3E* binding to Plexin-D1 elevates PIP_2 locally to activate *Arf6*, resulting in rapid focal adhesion disassembly (*Sakurai et al., 2011*). Since *Mtss1* I-BAR can interact with Plexin-D1 at the curved membrane, the local increase in PIP_2 in the curved membrane region may trigger signaling cascades. Although BAR-domain proteins play pivotal roles in membrane dynamics, a direct association between BAR-domain proteins and axon guidance receptors has not been extensively studied, and functional relevance *in vivo* is unclear. One example is the *srGAP2* protein, which has been studied and shown to bind directly with the SH3 domain of the *Robo1* guidance protein in cooperation with the F-BAR and RhoGAP domains (*Guez-Haddad et al., 2015*). Interestingly, in endothelial cells, Plexin-D1 forms a complex with SH3BP1, another small GTPase protein containing the N-BAR domain (*Tata et al., 2014*). Similar to the effect of *Mtss1* and Plexin-D1 complex formation via the I-BAR domain, SH3BP1 colocalized with Plexin-D1 at lamellipodia in a complex formed via the N-BAR domain and mediates *Sema3E*-induced cell collapse through *Rac1* activity regulation. However, in contrast to the effect of the *Mtss1* mutant lacking the I-BAR domain, which failed to change the cell morphology, SH3BP1 lacking N-BAR led to cell collapse. Moreover, *Sema3E* binding to Plexin-D1 caused SH3BP1 to be released from the

complex, whereas *Sema3E* did not interfere with the Plexin-D1-Mtss1 complex. In addition, the presence of *Mtss1* had no effect on the endocytosis of Plexin-D1 by *Sema3E* or on the ability of *Sema3E* to bind to Plexin-D1. Hence, it is plausible that *Mtss1* plays a role as a facilitator of Plexin-D1 trafficking rather than as a direct downstream signaling transducer such as SH3BP1. Because of the diverse roles played by *Sema3E*-Plexin-D1 across cell types, the effect of signaling induced by this guidance cue may be determined by distinct downstream molecules that share structural similarities in a relevant biological context. Another intriguing finding is the specific complex formation between Plexin-D1 and *Mtss1* in the present study. Plexin-D1 did not form a complex with other BAR-domain-containing proteins, srGAP2 and IRSP53, known to have a role in neurons. While we did not conduct an extensive examination, it is noteworthy that at least two other Plexin proteins were unable to form a complex with *Mtss1*. Therefore, it would be interesting to explore the structural characteristics underlying these interactions.

Variable axon projection defects in direct pathway MSNs mediated by *Sema3E*-Plexin-D1 signaling

To modulate movement information conveyed through basal ganglia circuitry, two distinct types of striatal MSNs send axonal projections to different targets: a direct-pathway MSN expresses the dopamine D1 receptor to promote movement, and an indirect-pathway MSN expresses the dopamine D2 receptor to inhibit movement (*Kreitzer and Malenka, 2008; Surmeier et al., 2007*). Because of these unique functional and anatomical features, decoding the distinct molecular properties of the two types of MSNs and the regulatory mechanisms involved in circuitry formation is important. A few previous transcriptome analyses have been performed with juvenile and adult mouse brains (*Heiman et al., 2008; Kronman et al., 2019; Lobo et al., 2006*), but an understanding of the molecular repertoire of each MSN during development is very limited. In the present study, *Mtss1* was identified as a selective molecule expressed in striatonigral projection neurons mediated by *Sema3E*-Plexin-D1 signaling, but its expression is limited to only the early striatonigral projection period; therefore, the previous transcriptome database in adults may have failed to identify *Mtss1* as a specific marker molecule in direct-pathway MSNs.

In this study, *Mtss1* expression was found to be relatively high during the perinatal period and then was dramatically downregulated by P7, by which time striatonigral projection has been completed (*Morello et al., 2015*). Consistent with a previous study showing that Plexin-D1-positive cells in the striatum were first detected on E14.5 (*van der Zwaag et al., 2002*), we found that its expression increased in the early postnatal stage. During a similar developing window in the striatonigral pathway, *Sema3E* was predominantly expressed in the GP and rTh/ZI, which is located in the route to the substantia nigra; therefore, the absence of repulsive *Sema3E*-Plexin-D1 signaling resulted in defects in striatonigral projection (*Burk et al., 2017; Chauvet et al., 2007; Ehrman et al., 2013*). However, we did not find ectopic projections, misguidance defects, or enlarged paths in *Mtss1*- or *Plxnd1*-knockout mice. Nevertheless, we observed fewer projections with aberrantly tangled patterns. These discrepancies may be explained by the following observations. First, because we used a genetic model to selectively label the striatonigral projections, we could detect abnormal phenotypes at a better specific resolution. Second, we noticed a certain degree of developmental retardation in the *Mtss1*- or *Plxnd1*-knockout neonates, even among those in the same litter; therefore, we strictly selected samples on the basis of body weight. However, despite the low striatonigral projection formation rate in the *Mtss1*-, *Plxnd1*-, or *Sema3e*-knockout mice, the adult mice showed a normal overall range of projection boundary size and width, suggesting that a decrease in repulsive signals in the mutants may have widened the descending projections. Third, the mouse genetic background may have led to the observed phenotypic discrepancies. We previously observed that certain vascular phenotypes were more evident in *Sema3e*-knockout mice with a 129SVE background than in those with a C57BL/6 background (*Oh and Gu, 2013b*), implying that relatively minor defects may vary depending on the genetic background.

Although *Sema3E*-Plexin-D1 has a similar mechanism of action as a common guidance cue in the nervous and vascular systems, it also exhibits completely different behavior in each system (*Oh and Gu, 2013a*). For example, the Plexin-D1-Npn1-VEGFR2 complex transmits an attractive signal upon *Sema3E* binding in specific neurons (*Bellon et al., 2010*), but endothelial cells still respond negatively to *Sema3E* despite the presence of all three receptors (*Oh and Gu, 2013b*). Interestingly,

Sema3E-Plexin-D1 utilizes Akt-mediated cytoskeletal dynamics for its signaling cascade in both neuronal and endothelial cells (Burk *et al.*, 2017; Moriya *et al.*, 2010), and various auxiliary molecules, such as SH3BP1, Arf6, and GIPC1, have been revealed in each cell (Burk *et al.*, 2017; Sakurai *et al.*, 2010; Tata *et al.*, 2014). However, only a few of these cofactors have shown a common molecular mechanism and expression by exchanging cells with each other, suggesting that Sema3E-Plexin-D1 signaling requires unique factors to perform different functions. Similarly, we identified Mtss1 as a downstream factor of the Sema3E-Plexin-D1 cue, but its function seems to be limited in neurons, at least *in vivo*. Therefore, it is necessary to elucidate whether Sema3E-Plexin-D1 signaling activates a specific pool of regulatory factors required for vascular development and to compare this with the results obtained in neurons, which will help us understand the underlying mechanism of specific molecule expression by guidance signaling. Furthermore, given the tremendous complexity of wiring in the central nervous system, it will be intriguing to discover new dual-function molecules similar to those in the Sema3E-Plexin-D1-Mtss1 complex that are involved in the formation of other circuits in the future.

Materials and methods

Mice

Plxnd1^{lox/lox} (*Plxnd1^{fl/fl}*) mice (Kim *et al.*, 2011) and *Sema3e^{+/-}* mice (Chauvet *et al.*, 2007) were maintained on a C57BL/6 (#000664, The Jackson Laboratory) background. Nestin-Cre (#003771), Tie2-cre (#008863), and *Drd1a*-tdTomato (#016204) mice were obtained from The Jackson Laboratory (Bar Harbor, USA) and maintained on the same background. The frozen sperm of *Mtss1^{lox/+}* mice were generously provided by Dr. Mineko Kengaku and rederived at the Laboratory Animal Resource Center in the Korea Research Institute of Bioscience and Biotechnology (Cheongju, Korea). All protocols for animal experiments were approved by the Institutional Animal Care and Use Committee of Korea Brain Research Institute (IACUC-18-00008, 20-00012). All experiments were performed according to the National Institutes of Health Guide for the Care and Use of Laboratory Animals and ARRIVE guidelines.

Cell lines and primary striatal neuron culture

COS7 (21651, Korean Cell Line Bank), HEK293T (CRL-3216, ATCC), HUVEC (CC-2935, Lonza), and HCMEC/D3 (SCC066, Millipore) cell lines were purchased from the indicated companies, and the cell culture media and culture conditions were as provided by the respective companies. All cell lines were initially authenticated by the company and were tested to be mycoplasma negative. Primary mouse striatal neurons were isolated from neonatal pups as described in a previous report with some modifications (Penrod *et al.*, 2011). Whole striatal tissues including the globus pallidus were digested with 20 units/ml papain (LS003124, Worthington, Lakewood, USA) diluted in dissection solution (5 mM MgCl₂ and 5 mM HEPES in 1× Hanks' balanced salt solution, pH 7.2) followed by multiple washes in inhibition solution (0.1% BSA and 0.1% Type II-O trypsin inhibitor diluted in dissection solution). The tissues were resuspended in neuronal plating medium (1 mM pyruvic acid, 0.6% glucose, and 10% heat-inactivated horse serum in Minimum Essential Medium with Earle's Salts) and triturated 50 times with a fire-polished Pasteur pipette. The dissociated neurons were centrifuged at 1000 × *g* for 5 min and resuspended in fresh neuronal plating media for cell counting. Then, the cells were plated on coverslips or culture dishes coated with 50 µg/ml poly-D-lysine (P6407, Sigma) and 1 µg/ml laminin (354232, Corning) at a density of 3 × 10⁴ cells/cm². After 4 hr of incubation at 37°C, the plating media were replaced with neuronal growth media (0.5 mM L-glutamine, B27 supplements in neurobasal medium [10888022, Gibco]), and a quarter of the media was replaced with fresh growth media every 3 d until harvest.

Plasmids

A pBK-CMV vector containing VSV-tagged human Plexin-D1 cDNA (Gu *et al.*, 2005) was recloned into a pCAG vector (pCAG-vsv-hPlexin-D1), and a Plexin-D1 construct lacking an ICD (amino acids deleted: 1299–1925) was generated by PCR-based mutagenesis (pCAG-vsv-hPlexin-D1ΔICD). To generate the pCAG-hPlexin-D1-GFP fusion construct, a GFP gene fragment was inserted at the C-terminus of the pCAG-vsv-hPlexin-D1 plasmid. pAptag-5-Sema3E vectors were reported previously (Chauvet *et al.*, 2007), and the mouse Plexin-D1 extracellular domain (amino acids: 1–1269) was amplified from

mouse Plexin-D1 cDNA and directly cloned into a pAptag-5 vector (pAptag5-mPlexin-D1-ECD). The human full-length Mtss1 expression construct was purchased from Origene (pCMV6-hMtss1, Cat# RC218273, USA), and Myc-tagged Mtss1 deletion constructs (Mtss1 Δ I-BAR [amino acids deleted: 1–250], Mtss1 Δ WH2 [amino acids deleted: 714–745], and Mtss1-I-BAR [amino acids: 1–250]) were generated by PCR-based mutagenesis. To generate full-length mouse Flag-Plexin-D1, SH3BP1-HA, and HA-srGAP2, each gene was isolated directly from the mouse brain cDNA library and cloned into pCAG vector with the tagging fragment. The mouse vsv-plexin-B2, mouse vsv-plexin-B3, and human pECE-M2-BAIAP2 (IRSP53-Flag) were purchased from Addgene (#68038, #68039, #31656, USA).

RNA sequencing analysis

RNA sequencing (RNA-seq) library preparation and sequencing were conducted at Ebiogen (Seoul, South Korea). Libraries were constructed using a NEBNext Ultra Directional RNA-seq Kit customized with mouse-specific oligonucleotides for rRNA removal. Directional mRNA-seq was conducted using the paired-end, 6 Gb read option of the Illumina HiSeq X10 system.

Bioinformatic analysis for RNA-seq

The entire analysis pipeline of RNA-seq was coded using R software (version 3.6), which was controlled by systemPipeR (version 1.18.2). The raw sequence reads were trimmed for adaptor sequences and masked for low-quality sequences using systemPipeR. Transcript quantification of the RNA-seq reads was performed with GenomicAlignments (version 1.20.1) using reads aligned with the *Mus musculus* transcriptome annotation using Rsubread (version 1.24.6). The fragments per kilobase of transcript per million mapped reads (FPKM) values were calculated using the fpkm function of DESeq2 (version 1.24.0) and were processed using the robust median ratio method. Transcript reads were normalized by the voom function of Limma (version 3.40.6). To determine if a transcript was differentially expressed (DE), EdgeR (version 3.26.7) calculated the results based on the normalized counts from entire sequence alignments. Significantly DE transcripts with a fold change greater than the raw FPKM value (>2) and adjusted p-value (<0.01) in all experimental comparisons were selected and used for further analysis. Gene annotations were added with an online database using Ensembl biomaRt (version 2.40.4), and visualization was performed using the R base code and gplots package (version 3.0.1.1). For DEG sets, hierarchical cluster analysis was performed using complete linkage and Euclidean distance to measure similarity. All data analysis and the visualization of DEGs were conducted using R version 3.0.2 (<https://www.r-project.org/>).

Quantitative reverse transcription PCR (qRT-PCR)

Total RNA was extracted from dissected tissue using TRIzol (15596026, Thermo). cDNA was synthesized from 200 ng of total RNA with a QuantiTect Reverse Transcription Kit (205313, QIAGEN). Quantitative PCRs were carried out in triplicate using SYBR Green I Master Mix (S-7563, Roche) on a LightCycler 480 system (Roche). Expression was calculated using the $2^{-\Delta\Delta Ct}$ method with *Gapdh* as a reference. The following primers were used (forward primer and reverse primer, respectively): *Plxnd1*: 5'-CTAGAGATCCAGCGCCGTTT, 5'-GGCACTCGACAGTTGGTACA, *Mtss1*: 5'-CCTTTCCC TCATTGCCTGCCT, 5'-TCTGAGATGACGGGAACATGCC, and *Gapdh*: 5'-TGACGTGCCGCCTGGA GAAAC, 5'-CCGGCATCGAAGG TGGAAGAG.

Transfection

DNA expression constructs were transfected into COS7 or HEK293T cells by Lipofectamine 2000 (11668019, Invitrogen) in OPTI-MEM (31985-070, Gibco) for 4 hr according to the manufacturer's instructions and then replaced with normal culture media until the next procedure. For imaging analysis, 0.5 μ g of DNA was transfected into COS7 cells (1×10^4 cells/cm²) cultured on coverslips in a 12-well plate. For biochemical analysis, 4 μ g of DNA was transfected into HEK293T cells (3×10^4 cells/cm²) cultured on a 10 cm dish. To achieve high transfection efficiency into primary neurons, the nucleofection technique using a Lonza Amaxa Nucleofector was performed following the manufacturer's instructions (Basic Nucleofector Kit for Primary Mammalian Neurons, VAPI-1003). To transfect into neurons, 4 μ g of expression constructs were added to at least 1×10^6 isolated neuronal cells for each electroporation, and the transfected cells were plated and cultured as described in the previous section.

Alkaline phosphatase (AP)-conjugated ligand preparation and binding analysis

AP-conjugated Sema3E and Plexin-D1-ECD ligands were generated in HEK293T cells, and ligand binding experiments were performed as described in previous reports (Chauvet *et al.*, 2016; Chauvet *et al.*, 2007). Briefly, the AP-conjugated expression construct was transfected into cells by Lipofectamine 2000 and cultured overnight in Dulbecco's modified Eagle's medium containing 10% fetal bovine serum (FBS). Then, the medium was replaced with OPTI-MEM and harvested at 5 d post transfection. The collected conditioned medium was filtered to increase the ligand concentration.

To measure the binding ability of AP-Sema3E to the Plexin-D1 receptor, COS7 cells on a six-well plate were transfected with each expression vector and cultured for 24 hr. The next day, the cells were washed in HBHA buffer (1× HBSS, 0.5 mg/ml BSA, 0.5% sodium azide, and 20 mM HEPES [pH 7.0]) and incubated with 2 nM AP or AP-Sema3E for 1 hr at room temperature (RT). After seven washes in the HBHA buffer, the cells were lysed in 1% Triton X-100 and 10 mM of Tris-HCl (pH 8.0), and the supernatant was obtained by centrifugation at 13,000 × *g* for 10 min. The lysates were heat-inactivated at 65°C for 10 min, each lysate was used for AP concentration using a BioMate 3S spectrophotometer (Thermo Scientific), and the amount of protein was measured by BCA assay.

For AP-conjugated ligand binding analysis of tissues, 20- μ m-thick cryosections were fixed in cold methanol for 8 min and preincubated in 1× phosphate-buffered saline (PBS) containing 4 mM MgCl₂ and 10% FBS for 1 hr. Next, a binding solution (1× PBS-MgCl₂ and 20 mM HEPES, pH 7.0) containing 2 nM AP-Sema3E was applied, and sections were incubated for 2 hr at RT. After five washes in 1× PBS-MgCl₂, the sections were briefly soaked in acetone-formaldehyde fixative (60% acetone, 1.1% formaldehyde, and 20 mM HEPES, pH 7.0) and heat-inactivated in 1× PBS at 65°C for 2 hr. Next, the sections were incubated in AP buffer (NBT/BCIP tables, 11697471001, Roche) until clear purple precipitation was observed at RT. For quantification, three brain sections per animal were analyzed and averaged. For the AP-Sema3E binding analysis of growth cones, MSNs grown for 6 d on glass coverslips were washed in 1× PBS, immediately fixed in cold methanol for 5 min, and blocked in TBS buffer (100 mM TBS, 4 mM MgCl₂, 4 mM CaCl₂, pH 7.4) with 10% FBS at RT for 1 hr. The MSNs were then incubated in 0.5 nM AP-Sema3E ligand diluted in blocking solution at RT for 1 hr. After five washes in TBS buffer, the MSNs were fixed in acetone/formaldehyde solution, heat-inactivated, and incubated in AP buffer as described above.

AP treatment of HUVECs and HCMEC/D3 cells

HUVECs were purchased from Lonza, and the HCMEC/D3 cell line was obtained from Millipore. The cell culture media and culture conditions used followed the information provided by the respective companies. Cultured HUVECs and HCMEC/D3 cells were treated with 2 nM AP or AP-Sema3E for 24 hr. Then, the cells were lysed and prepared for western blotting as described below.

Immunoblotting

Brain tissue was collected in radioimmunoprecipitation assay (RIPA) buffer (50 mM Tris-HCl [pH 8.0], 150 mM NaCl, 1% NP-40, and 1% sodium deoxycholate) with a protease inhibitor cocktail (78444, Thermo Fisher Scientific), and protein amounts were quantified using a BCA protein assay kit (23227, Thermo Fisher Scientific). A total of 40 μ g of protein was loaded into each well of a sodium dodecyl sulfate (SDS) polyacrylamide gel, after which it was separated and transferred to a polyvinylidene fluoride membrane (IPVH00010, Merck) at 100 V for 90 min. All membranes were blocked in Everyblot blocking buffer (12010020, Bio-Rad) for 1 hr and probed overnight with primary antibodies in blocking buffer at 4°C. The primary antibodies included the following: anti-Mtss1 (1:1000, Novus, NBP2-24716), anti-Plexin-D1 (1:1000, AF4160, R&D Systems), anti- β -actin (1:5000, 5125S, Cell Signaling), anti-Myc (1:1000, 2276S, Cell Signaling), anti-vsv (1:1000, ab3861, Abcam), anti-Sema3E (1:500, LS-c353198, LSBio), anti-p-AKT (1:1000, 9271, Cell Signaling), and anti-AKT (1:1000, 9272S, Cell Signaling). The membranes were incubated in TBST, and the appropriate horseradish peroxidase (HRP)-conjugated secondary antibodies and bands were developed with enhanced chemiluminescence using Fusion FX7 (Vilber, Germany) and then analyzed using ImageJ software.

Immunoprecipitation

HEK293T cells were transfected with Lipofectamine 2000, and after 24 hr, they were lysed in a buffer consisting of 100 mM Tris-HCl (pH 7.5), 100 mM EDTA, 150 mM NaCl, and 1% Triton X-100 with freshly added phosphate and protease inhibitors. The cell lysates were centrifuged at $13,000 \times g$ for 10 min at 4°C, and supernatants were incubated with antibodies (1:200) at 4°C overnight. Then, the protein lysates were incubated with magnetic beads for 1 hr at 4°C. Next, the beads were washed five times with lysis buffer, and the bound proteins were eluted with a 2× SDS sample buffer by heating the beads at 95°C for 5 min. The samples were then analyzed by SDS-PAGE and western blotting. The following antibodies were purchased from commercial sources: anti-Myc (1:1000, 2276S, Cell Signaling), anti-vsv (1:1000, ab3861, Abcam), anti-Mtss1 (1:1000, NBP2-24716, Novus), anti-Plexin-D1 (1:1000, AF4160, R&D Systems), and anti-β-actin (1:5000, 5125S, Cell Signaling).

Protein-protein interaction assay

The I-BAR domain of human Mtss1 was purchased from Sino Biological (Cat# 13085-H10E). The human Plexin-D1 cytosolic domain was prepared. Briefly, the coding sequence of the human PLXND1 (NM_105103.3) cytosolic domain (amino acid residue 1297–1925; hPLXND1_Cyto) was subcloned into the mammalian expression vector CAGs-MCS EEV (SBI, Palo Alto, CA) in-frame fused with a C-terminal twin strep tag (SAWSHPQFEKGGGSGGGGSAWSHPQFEK). HEK293 G_nT1⁻ cells were transfected with the PLXND1 expression vector and grown in FreeStyle 293 Expression Medium supplemented with 2% (v/v) FBS in a humidified CO₂ incubator (35°C, 5% CO₂) with shaking at 150 rpm for 3 d. Cells were harvested, resuspended in resuspension buffer (500 mM NaCl, 10 mM Tris-HCl, pH 8.0, 5% [v/v] glycerol, 3 mM β-mercaptoethanol, protease inhibitor cocktail [Roche], 0.4 mg/ml DNase I [GOLDBIO]), and disrupted by using a Dounce homogenizer followed by sonication. After the removal of cell debris by centrifugation, the cell lysate was loaded onto pre-equilibrated Strep-Tactin XT 4Flow resin (IBA Lifesciences GmbH, Germany) and washed with wash buffer (500 mM NaCl, 10 mM Tris-HCl, pH 8.0, 5% [v/v] glycerol, 3 mM β-mercaptoethanol). hPLXND1_Cyto with a twin strep tag was eluted with elution buffer (50 mM biotin, 500 mM NaCl, 10 mM Tris-HCl, pH 8.0, 5% [v/v] glycerol, 3 mM β-mercaptoethanol) and further purified by using size-exclusion chromatography on a size-exclusion column (Superdex 200) equilibrated with FPLC buffer (150 mM NaCl, 20 mM Tris, pH 8.0, 10% glycerol [v/v], 2 mM DTT). To obtain the tag-free hPLXND1_Cyto proteins, the C-terminal twin strep tag was removed by incubating with the 3C protease (Takara Bio, Japan; 1.5 unit/50 mg protein) and ran on a size-exclusion column. To analyze direct binding, Mtss1-I-BAR with Plxind-D1-ICD was mixed in binding buffer (50 mM Tris-HCl, 0.1% Triton X-100) and incubated overnight at 4°C. The mixed proteins were then incubated with Ni-NTA beads for 1 hr at 4°C. Next, the beads were washed five times with binding buffer, and the bound protein was eluted with 2× SDS sample buffer by heating the beads at 95°C for 5 min. The samples were then analyzed by SDS-PAGE and stained with Coomassie blue solution. After washing with water five times, the stained gels were visualized using a Bio-Rad instrument.

Cell surface biotinylation and endocytosis analysis

Transfected COS7 cells on a 100 mm dish were biotinylated by incubation in 1 mg/ml NHS-SS-Biotin (21331, Thermo Scientific), diluted in 1× PBS containing 1 mM MgCl₂ and 0.1 mM CaCl₂ (PBS-MC) for 15 min, washed in PBS-MC containing 10 mM glycine at least three times, and then rinsed in ice-cold PBS-MC twice at 4°C. For the negative control, the cells were incubated in stripping buffer (50 mM glutathione, 75 mM NaCl, 10 mM EDTA, 75 mM NaOH, and 1% bovine serum albumin [BSA]) and washed twice in PBS-MC. For the neutralization of glutathione, the cells were incubated in PBS-MC containing 50 mM iodoacetamide (I1149, Sigma) three times. All biotinylated or stripped cells were lysed in ice-cold RIPA buffer (50 mM Tris-HCl [pH 8.0], 150 mM NaCl, 1% NP-40, and 1% sodium deoxycholate) with a protease inhibitor cocktail, and 100 μg of protein extracts was incubated in prewashed streptavidin agarose resin (20357, Thermo Scientific) overnight and rotated throughout. Cell extracts were serially washed in bead-washing solution (Solution A: 150 mM NaCl, 50 mM Tris-HCl [pH 7.5], and 5 mM EDTA; Solution B: 500 mM NaCl, 50 mM Tris-HCl [pH 7.5], and 5 mM EDTA; Solution C: 500 mM NaCl, 20 mM Tris-HCl [pH 7.5], and 0.2% BSA) followed by another wash in 10 mM Tris-HCl (pH 7.5). The bound biotinylated proteins were recovered by adding 2× sample buffer and boiling extracts for 5 min, and then the supernatants were subjected to western blotting.

To analyze endocytic protein levels, cells were incubated for 25 min at 37°C in the presence of prewarmed culture media with 2 nM AP or AP-Sema3E ligands after surface biotinylation. Then, the biotinylated proteins remaining on the cell surface were removed by stripping procedures, and the rest of the experiment was continued as described in the above section. Except for those used in the ligand stimulation process, all reagents were prechilled, and experiments were performed in an ice or cold chamber.

Immunostaining

For immunocytochemistry, cultured cells or neurons on coverslips were fixed in 4% paraformaldehyde (PFA) for 5 min and washed several times in PBS. Then, the cells were permeabilized in PBST (PBS containing 0.1% Triton X-100) for 5 min, blocked with 5% horse serum in PBST for 60 min at RT, and incubated with primary antibodies diluted in blocking solution overnight at 4°C. The next day, the samples were washed with PBST three times and incubated for 1 hr with Alexa Fluor 488-, 594-, or 647-conjugated secondary antibodies (1:1000, Thermo). To enable visualization of the F-actin, Alexa Fluor-conjugated phalloidin (1:50, Thermo) was added during the secondary antibody incubation. After being washed again with PBST, the samples were mounted with Prolong Diamond antifade solution containing DAPI (P36962, Thermo). Image processing was performed using ImageJ or Adobe Photoshop (Adobe Photoshop CC2019) under identical settings. All other immunostaining procedures were the same as those described above. The following primary antibodies for immunocytochemistry were used: anti-vsv (1:1000, ab3861, Abcam), anti-Myc (1:1000, 2276S, Cell Signaling), phalloidin Alexa Fluor 488 (1:50, A12379, Thermo), phalloidin Alexa Fluor 647 (1:100, A22287, Thermo), anti-RFP (1:1000, ab62341, Abcam), anti-RFP (1:1000, MA5-15257, Thermo), anti-Tau (1:500, sc-1995, Santa Cruz), and anti-alpha-tubulin (1:1000, T5168, Sigma). Images were collected using a Nikon Eclipse Ti-U microscope (Nikon, Japan), Leica TCS SP8 Confocal Microscope (Leica, Germany), or Structured Illumination Microscope (Nikon).

For immunohistochemistry with tissue samples, brains were fixed in 4% PFA overnight and equilibrated with 20% sucrose in 1× PBS. Mouse brain sections were cut into 20 µm slices on a cryostat (Leica Microsystems Inc, Buffalo Grove, IL). Mouse brain sections were permeabilized in PBST (PBS containing 0.2% Triton X-100) for 10 min, blocked with 2% BSA and 5% normal donkey serum in PBST for 60 min at RT, and then incubated in primary antibodies diluted with 2% BSA in PBST overnight at 4°C. The following primary antibodies were used: anti-Mtss1 (1:1000, NBP2-24716, Novus), anti-RFP (1:1000, MA5-15257, Thermo), anti-neurofilament (1:500, 2H3, Hybridoma Bank), anti-CD31 (1:500, 553370, BD Biosciences), and anti-cleaved caspase 3 (1:1000, 9661, Cell Signaling). After being washed with PBS/0.2% Tween 20 (PBST) three times, sections were incubated for 1 hr with Alexa Fluor 488-, 594-, or 647-conjugated secondary antibodies (1:1000, Invitrogen). For negative controls, brain sections were stained with secondary antibodies only. Image processing was performed using ImageJ or Adobe Photoshop (Adobe Photoshop CC2019).

Growth cone collapse and neurite length analysis

For the growth cone collapse assay, striatal neurons at DIV3 were incubated with 5 nM AP or AP-Sema3E 3 for 25 min. For the preservation of the growth cone structure, 8% PFA was directly added to cultured neurons to equalize at 4% PFA for 10 min at 37°C, and subsequently, another 5 min round of 4% PFA fixation was performed on ice before the immunostaining procedure. Growth cone images were collected from tdT-positive neurons using a Structured Illumination Microscope (SIM, Nikon), and collapsed growth cones were determined blindly. Growth cones with broad lamellipodia were considered intact, whereas those with a few filopodia lacking lamellipodia were defined as collapsed according to previous guidelines (*Oh and Gu, 2013b*).

For measurement of neurite length, dissociated striatal neurons were cultured in the presence of 5 nM ligands and immunostained as described in the above section. The neurons were imaged by a fluorescence microscope (Nikon ECLIPSE Ti-U), and the longest neurite length from tdT-positive neurons was determined using ImageJ software. The neurites that formed a network with another neurite and those whose longest protrusions were smaller than twice the cell body diameter were excluded from measurement according to previous guidelines (*Chauvet et al., 2016*). For quantification of the degree of colocalization, Pearson's correlation coefficients were calculated using the manufacturer's software (Nikon, NIS-Elements software).

In situ hybridization (ISH)

ISH was performed under RNase-free conditions as described in a previous study (Ding et al., 2012). After fixation in 4% PFA for 20 min, 20- μ m-thick cryosections were preincubated in hybridization buffer (5 \times Denhardt's solution, 5 \times saline sodium citrate [SSC], 50% formamide, 0.25 mg/ml Baker yeast tRNA, and 0.2 mg/ml salmon sperm DNA) for 2 hr at RT. Next, the sections were hybridized in the same buffer containing the indicated digoxigenin-conjugated riboprobe at 60°C overnight. After hybridization, the sections were washed in a serial SSC buffer and formamide solution and then preincubated in buffer 1 (100 mM Tris-HCl, pH 7.5, 150 mM NaCl) with a 1% blocking reagent (Roche) for 1 hr at RT. Next, the sections were incubated with sheep anti-digoxigenin-AP antibody (1:3000, Roche) for 90 min at RT, washed in buffer 1, and then incubated in AP buffer (100 mM Tris-HCl, pH 9.5; 100 mM NaCl; and 5 mM MgCl₂) containing 4-nitro blue tetrazolium chloride (NBT, Roche), 5-bromo-4-chloro-3-indolyl-phosphate (BCIP, Roche), and levamisole (1359302, Sigma) until purple precipitates were observed. After mounting them with coverslips, the samples were analyzed using confocal laser-scanning microscopy with a Nikon Eclipse Ti-U Microscope or Leica TCS SP8 Confocal Microscope. For double fluorescence ISH, the tyramide signal amplification method with minor modifications was used according to the manufacturer's instructions (NEL753001KT, PerkinElmer). The following anti-sense riboprobes were used: *Plxnd1* (Ding et al., 2012), *Sema3e* (Gu et al., 2005), and *Mtss1* (Allen Brain Atlas, Probe RP_040604_01_B06).

Live-cell imaging

Isolated striatal neurons were transfected with an expression plasmid, as described in the above section, and were plated onto a 35 mm confocal dish (211350, SPL Life Sciences) at a density of 1×10^4 cells/cm². At DIV6, time-lapse imaging was performed in a stage-top cell incubator (37°C with 5% CO₂ supplied). Images were acquired at 1 s intervals for 3 min using a Nikon A1-Rsi confocal microscope. To quantify Plexin-D1-GFP trafficking, time-lapse images were analyzed using Particle Tracking Recipe in AIVIA microscopy image analysis software (Aivia Inc).

Golgi staining and dendrite analysis

Golgi staining was conducted according to the manufacturer's protocol (FD Rapid GolgiStain Kit [PK401A, FD NeuroTechnologies, Inc]). In brief, P5 mouse brains were immersed in a staining solution for 2 wk before being transferred to a wash solution for 4 d. Then, 100 μ m slices were obtained using a vibratome and collected on gelatin-coated slides. During the staining process, the slices were washed twice with distilled water for 4 min, immersed in the staining solution for 10 min, and then washed again. The slices were then dehydrated, cleared in xylene three times for 4 min, mounted with Eukitt Quick-hardening mounting medium (Sigma, 03989), and imaged by light microscopy with Z-stack. Image processing was performed using NeuroLucida360 software in 3D analysis.

Whole-embryo immunostaining and clearance

Mouse embryos were fixed in 4% PFA overnight at 4°C and washed three times in PBS. Then, the embryos were permeabilized in PBST (PBS containing 1% Triton X-100) for 2 hr at RT, incubated in blocking solution (75% PBST, 20% dimethyl sulfoxide, 5% normal goat serum) for 3 hr at RT, and incubated in anti-CD31 (1:500, company name) diluted in the blocking solution at RT. After 3 d, the embryos were washed with PBST for 8 hr and incubated with Alexa Fluor 488-conjugated secondary antibody (1:500, Thermo) for 2 d at RT. After washing again with PBST for 8 hr, the embryos were cleared with ethyl cinnamate (ECi; Cat# 112372, Sigma) according to a previous protocol (Klingberg et al., 2017). Briefly, the embryos were subjected to serial dehydration with ethanol (EtOH) (30, 50, and 70% EtOH, pH 9.0 with 2% Tween 20, followed by twice 100% EtOH). The solutions were changed every 12 hr and incubated at 4°C. The samples were transferred to ECi and incubated at RT with gentle shaking until they became transparent, and cleared samples were stored in ECi at RT until imaging. All clearing procedures were performed in the dark. A Dragonfly 502w (Andor Technology) was used for imaging, and Imaris x64 9.6.1 (Bitplane) was used for image reconstruction.

Dil injection and imaging

For the tracing of the neural projection, small crystals of Dil (1.1-dioctadecyl-3,3,3-tetramethyl-indocarbocyanine perchlorate, Sigma) were inserted into the thalamus of an E16.5 mouse brain fixed in 4%

PFA overnight and sealed with 2% agarose melt in 1× PBS. Then, the brain was incubated in 4% PFA at 37°C for 2 wk and divided into 100 μm thick sections by a vibratome (Leica VT200S). Serial brain slices were immediately collected, and Dil-stained sections were imaged using a fluorescence microscope (Nikon Eclipse Ti-U). To sparsely label the striatonigral projection, Dil crystals were injected into the dorsal striatum of P5 mouse brain and incubated for a month or so under the same conditions as described above. Afterward, the tissue was sectioned into 100-μm-thick slices using a vibratome (Leica VT200S). Z-stack images were obtained by using Leica TCS SP8 Confocal Microscope, and the 3-D images were reconstructed utilizing Leica Application Suite X, an image analysis software.

Striatonigral projection analysis

For the analysis of striatonigral projections, P5 or P30 brains from wild-type (*Drd1a-tdT; Mtss1^{fl/fl}*), *Mtss1* cKO (*Drd1a-tdT; Nes-cre; Mtss1^{fl/fl}*), or *Plxnd1* cKO (*Drd1a-tdT; Nes-cre; Plxnd1^{fl/fl}*) mice were fixed in 4% PFA overnight and embedded in a 4% agarose block melt in PBS after being washed with PBS three times. Then, the areas of interest in the brain were divided into 100-μm-thick sections by a vibratome (Leica VT200S). Serial brain slices were immediately collected and mounted with Prolong Diamond antifade solution containing DAPI (P36962, Thermo). The sections were imaged with a fluorescence microscope (Nikon Eclipse Ti-U). To analyze the guidance phenotype in the striatonigral projections, we quantified the number of axon bundles intersecting with others between the globus pallidus (Gp) and the entopeduncular nucleus (EP). Since some mutants within the same litter occasionally displayed significant developmental delays, we selectively chose samples from mutant littermates with ±5% body weight variance for a reliable phenotypic assessment.

Quantification and statistical analysis

The estimate of variance was determined by the standard error of the mean (SEM), and statistical significance was set at $p < 0.05$. All data were tested with a Gaussian distribution using the Shapiro–Wilk test before statistical analysis. Pairwise comparisons were performed using the two-tailed Student's *t*-test or Mann–Whitney test, and multiple-group analyses were conducted with one-way or two-way ANOVA with Tukey's or Bonferroni's multiple comparisons test or Kruskal–Wallis test with Dunn's multiple comparisons test. For the growth cone collapse assay, the χ^2 test was used as previously reported (Burk *et al.*, 2017). For the quantification of colocalization, the images were analyzed using the Jacop plugin in ImageJ (National Institutes of Health, Bethesda, MD). Statistical data on colocalization were obtained using Costes' randomization based on the colocalization module, as previously described (Bolte and Cordelières, 2006). Statistical analyses were performed with Prism 9 (GraphPad Software). At least three pairs of mice were used per experiment for all histological analyses. For the quantification of image data, at least three brain sections per animal were collected and analyzed. All data analyses were performed by an investigator blinded to the groups. No statistical methods were used to predetermine sample sizes, but our sample sizes were similar to those generally employed in the field.

Acknowledgements

We thank Drs. Ayal Ben-Zvi, Soonmoon Yoo, and Chenghua Gu for reading the manuscript and providing critical advice; Dr. Chenghua Gu for providing *Sema3e* and *Plxnd1-flox* mice; Drs. Mineko Kengaku and Masayoshi Mishina for providing *Mtss1-flox* mice; Juhyun Lee for helping with quantification; the Advanced Neural Imaging Center in KBRI for image analysis. This research was supported by the KBRI basic research program of the Korea Brain Research Institute funded by the Ministry of Science and ICT (KBRI 23-BR-01-02), the National Research Foundation (NRF) funded by the Korean government (NRF-2014R1A1A2058234), the Bio & Medical Technology Development Program of the NRF & funded by the Korean government (MSIT) (NRF-2020M3E5D9079766 and NRF-2022M3E5E8017701) to WO, and the Young Researcher Program of the National Research Foundation (NRF) funded by the Korean government (MSIT) (2020R1C1C1010509) to NK.

Additional information

Funding

Funder	Grant reference number	Author
Korea Brain Research Institute	KBRI 23-BR-01-02	Won-Jong Oh
National Research Foundation of Korea	NRF-2014R1A1A2058234	Won-Jong Oh
National Research Foundation of Korea	NRF-2020M3E5D9079766	Won-Jong Oh
National Research Foundation of Korea	NRF-2022M3E5E8017701	Won-Jong Oh
National Research Foundation	Young Researcher Program 2020R1C1C1010509	Namsuk Kim

The funders had no role in study design, data collection and interpretation, or the decision to submit the work for publication.

Author contributions

Namsuk Kim, Data curation, Software, Formal analysis, Funding acquisition, Validation, Investigation, Visualization, Methodology, Writing - review and editing; Yan Li, Data curation, Software, Formal analysis, Validation, Investigation, Visualization, Methodology; Ri Yu, Data curation, Formal analysis, Validation, Visualization, Methodology; Hyo-Shin Kwon, Data curation, Formal analysis, Visualization, Methodology; Anji Song, Data curation, Formal analysis, Visualization; Mi-Hee Jun, Ji Hyun Lee, Data curation; Jin-Young Jeong, Data curation, Visualization; Hyun-Ho Lim, Data curation, Writing - review and editing; Mi-Jin Kim, Resources; Jung-Woong Kim, Resources, Data curation, Visualization, Writing - review and editing; Won-Jong Oh, Conceptualization, Resources, Data curation, Software, Formal analysis, Supervision, Funding acquisition, Validation, Investigation, Visualization, Methodology, Writing - original draft, Project administration, Writing - review and editing

Author ORCIDs

Namsuk Kim  <http://orcid.org/0000-0001-5043-0293>

Yan Li  <http://orcid.org/0000-0001-5276-1053>

Hyun-Ho Lim  <http://orcid.org/0000-0002-5477-5640>

Won-Jong Oh  <http://orcid.org/0000-0001-8867-7814>

Ethics

All protocols for animal experiments were approved by the Institutional Animal Care and Use Committee of Korea Brain Research Institute (IACUC-18-00008, 20-00012). All experiments were performed according to the National Institutes of Health Guide for the Care and Use of Laboratory Animals and ARRIVE guidelines.

Decision letter and Author response

Decision letter <https://doi.org/10.7554/eLife.96891.sa1>

Author response <https://doi.org/10.7554/eLife.96891.sa2>

Additional files

Supplementary files

- MDAR checklist

Data availability

The accession number for the RNA-Seq data reported in the present study is GSE196558.

The following datasets were generated:

Author(s)	Year	Dataset title	Dataset URL	Database and Identifier
W-J Oh	2022	Axon guidance signal ensures neurite growth pace while sensitizing repulsive cues through induction of a dual function facilitator	https://www.ncbi.nlm.nih.gov/geo/query/acc.cgi?acc=GSE196558	NCBI Gene Expression Omnibus, GSE196558
W-J Oh	2023	Axon guidance signal ensures neurite growth pace while sensitizing repulsive cues through induction of a dual function facilitator	https://www.mousemine.org/mousemine/report.do?id=89860228&trail=%7c89860228	MouseMine, GSE196558

References

- Ade KK, Wan Y, Chen M, Gloss B, Calakos N. 2011. An improved BAC transgenic fluorescent reporter line for sensitive and specific identification of striatonigral medium spiny neurons. *Frontiers in Systems Neuroscience* **5**:32. DOI: <https://doi.org/10.3389/fnsys.2011.00032>, PMID: 21713123
- Aghajanian H, Choi C, Ho VC, Gupta M, Singh MK, Epstein JA. 2014. Semaphorin 3d and semaphorin 3e direct endothelial motility through distinct molecular signaling pathways. *The Journal of Biological Chemistry* **289**:17971–17979. DOI: <https://doi.org/10.1074/jbc.M113.544833>, PMID: 24825896
- Arvanitis DN, Jungas T, Behar A, Davy A. 2010. Ephrin-B1 reverse signaling controls a posttranscriptional feedback mechanism via miR-124. *Molecular and Cellular Biology* **30**:2508–2517. DOI: <https://doi.org/10.1128/MCB.01620-09>, PMID: 20308325
- Bai G, Chivatakarn O, Bonanomi D, Lettieri K, Franco L, Xia C, Stein E, Ma L, Lewcock JW, Pfaff SL. 2011. Presenilin-dependent receptor processing is required for axon guidance. *Cell* **144**:106–118. DOI: <https://doi.org/10.1016/j.cell.2010.11.053>, PMID: 21215373
- Bellon A, Luchino J, Haigh K, Rougon G, Haigh J, Chauvet S, Mann F. 2010. VEGFR2 (KDR/Flk1) signaling mediates axon growth in response to semaphorin 3E in the developing brain. *Neuron* **66**:205–219. DOI: <https://doi.org/10.1016/j.neuron.2010.04.006>, PMID: 20434998
- Bolte S, Cordelières FP. 2006. A guided tour into subcellular colocalization analysis in light microscopy. *Journal of Microscopy* **224**:213–232. DOI: <https://doi.org/10.1111/j.1365-2818.2006.01706.x>, PMID: 17210054
- Bonanomi D, Valenza F, Chivatakarn O, Sternfeld MJ, Driscoll SP, Aslanian A, Lettieri K, Gullo M, Badaloni A, Lewcock JW, Hunter T, Pfaff SL. 2019. p19RhoGAP filters competing signals to resolve axon guidance conflicts. *Neuron* **102**:602–620. DOI: <https://doi.org/10.1016/j.neuron.2019.02.034>, PMID: 30902550
- Burk K, Mire E, Bellon A, Hocine M, Guillot J, Moraes F, Yoshida Y, Simons M, Chauvet S, Mann F. 2017. Post-endocytic sorting of Plexin-D1 controls signal transduction and development of axonal and vascular circuits. *Nature Communications* **8**:14508. DOI: <https://doi.org/10.1038/ncomms14508>, PMID: 28224988
- Chauvet S, Cohen S, Yoshida Y, Fekrane L, Livet J, Gayet O, Segu L, Buhot MC, Jessell TM, Henderson CE, Mann F. 2007. Gating of Sema3E/PlexinD1 signaling by neuropilin-1 switches axonal repulsion to attraction during brain development. *Neuron* **56**:807–822. DOI: <https://doi.org/10.1016/j.neuron.2007.10.019>, PMID: 18054858
- Chauvet S, Mire E, Mann F. 2016. Semaphorin signaling, methods and protocols. *Methods in Molecular Biology* **1493**:223–235. DOI: <https://doi.org/10.1007/978-1-4939-6448-2>
- Chen Y, Aardema J, Corey SJ. 2013. Biochemical and functional significance of F-BAR domain proteins interaction with WASP/N-WASP. *Seminars in Cell & Developmental Biology* **24**:280–286. DOI: <https://doi.org/10.1016/j.semcdb.2013.01.005>, PMID: 23384583
- Dent EW, Gupton SL, Gertler FB. 2011. The growth cone cytoskeleton in axon outgrowth and guidance. *Cold Spring Harbor Perspectives in Biology* **3**:a001800. DOI: <https://doi.org/10.1101/cshperspect.a001800>, PMID: 21106647
- Ding JB, Oh WJ, Sabatini BL, Gu C. 2012. Semaphorin 3E–Plexin-D1 signaling controls pathway-specific synapse formation in the striatum. *Nature Neuroscience* **15**:215–223. DOI: <https://doi.org/10.1038/nn.3003>
- Droz B, Koenig HL, Giamberardino LD. 1973. Axonal migration of protein and glycoprotein to nerve endings. I. Radioautographic analysis of the renewal of protein in nerve endings of chicken ciliary ganglion after intracerebral injection of [3H]lysine. *Brain Research* **60**:93–127. DOI: [https://doi.org/10.1016/0006-8993\(73\)90852-4](https://doi.org/10.1016/0006-8993(73)90852-4)
- Dupin I, Lokmane L, Dahan M, Garel S, Studer V. 2015. Subrepellent doses of Slit1 promote Netrin-1 chemotactic responses in subsets of axons. *Neural Development* **10**:5. DOI: <https://doi.org/10.1186/s13064-015-0036-8>, PMID: 25888985
- Dupont S, Wickström SA. 2022. Mechanical regulation of chromatin and transcription. *Nature Reviews. Genetics* **23**:624–643. DOI: <https://doi.org/10.1038/s41576-022-00493-6>, PMID: 35606569

- Ehrman LA**, Mu X, Waclaw RR, Yoshida Y, Vorhees CV, Klein WH, Campbell K. 2013. The LIM homeobox gene *Isl1* is required for the correct development of the striatonigral pathway in the mouse. *PNAS* **110**:E4026–E4035. DOI: <https://doi.org/10.1073/pnas.1308275110>, PMID: 24082127
- Franze K**. 2020. Integrating chemistry and mechanics: The forces driving axon growth. *Annual Review of Cell and Developmental Biology* **36**:61–83. DOI: <https://doi.org/10.1146/annurev-cellbio-100818-125157>, PMID: 32603614
- Fukuhara K**, Imai F, Ladle DR, Katayama K, Leslie JR, Arber S, Jessell TM, Yoshida Y. 2013. Specificity of monosynaptic sensory-motor connections imposed by repellent *Sema3E*-*PlexinD1* signaling. *Cell Reports* **5**:748–758. DOI: <https://doi.org/10.1016/j.celrep.2013.10.005>
- Gerfen CR**, Surmeier DJ. 2011. Modulation of striatal projection systems by dopamine. *Annual Review of Neuroscience* **34**:441–466. DOI: <https://doi.org/10.1146/annurev-neuro-061010-113641>, PMID: 21469956
- Giehl K**, Keller C, Muehlich S, Goppelt-Strube M. 2015. Actin-mediated gene expression depends on *RhoA* and *Rac1* signaling in proximal tubular epithelial cells. *PLOS ONE* **10**:e0121589. DOI: <https://doi.org/10.1371/journal.pone.0121589>, PMID: 25816094
- Gu C**, Yoshida Y, Livet J, Reimert DV, Mann F, Merte J, Henderson CE, Jessell TM, Kolodkin AL, Ginty DD. 2005. *Semaphorin 3E* and *plexin-D1* control vascular pattern independently of neuropilins. *Science* **307**:265–268. DOI: <https://doi.org/10.1126/science.1105416>, PMID: 15550623
- Guez-Haddad J**, Sporny M, Sasson Y, Gevorkyan-Airapetov L, Lahav-Mankovski N, Margulies D, Radzimanowski J, Opatowsky Y. 2015. The neuronal migration factor *srGAP2* achieves specificity in ligand binding through a two-component molecular mechanism. *Structure* **23**:1989–2000. DOI: <https://doi.org/10.1016/j.str.2015.08.009>, PMID: 26365803
- Harrington AW**, Ginty DD. 2013. Long-distance retrograde neurotrophic factor signalling in neurons. *Nature Reviews. Neuroscience* **14**:177–187. DOI: <https://doi.org/10.1038/nrn3253>, PMID: 23422909
- Hayn-Leichsenring G**, Liebig C, Miething A, Schulz A, Kumar S, Schwalbe M, Eiberger B, Baader SL. 2011. Cellular distribution of metastasis suppressor 1 and the shape of cell bodies are temporarily altered in *Engrailed-2* overexpressing cerebellar Purkinje cells. *Neuroscience* **189**:68–78. DOI: <https://doi.org/10.1016/j.neuroscience.2011.05.038>, PMID: 21651965
- Heiman M**, Schaefer A, Gong S, Peterson JD, Day M, Ramsey KE, Suárez-Fariñas M, Schwarz C, Stephan DA, Surmeier DJ, Greengard P, Heintz N. 2008. A translational profiling approach for the molecular characterization of CNS cell types. *Cell* **135**:738–748. DOI: <https://doi.org/10.1016/j.cell.2008.10.028>, PMID: 19013281
- Jung H**, Yoon BC, Holt CE. 2012. Axonal mRNA localization and local protein synthesis in nervous system assembly, maintenance and repair. *Nature Reviews. Neuroscience* **13**:308–324. DOI: <https://doi.org/10.1038/nrn3210>, PMID: 22498899
- Kawabata Galbraith K**, Fujishima K, Mizuno H, Lee SJ, Uemura T, Sakimura K, Mishina M, Watanabe N, Kengaku M. 2018. *MTSS1* regulation of actin-nucleating formin *DAAM1* in dendritic filopodia determines final dendritic configuration of Purkinje cells. *Cell Reports* **24**:95–106. DOI: <https://doi.org/10.1016/j.celrep.2018.06.013>, PMID: 29972794
- Kim J**, Oh WJ, Gaiano N, Yoshida Y, Gu C. 2011. *Semaphorin 3E*-*Plexin-D1* signaling regulates *VEGF* function in developmental angiogenesis via a feedback mechanism. *Genes & Development* **25**:1399–1411. DOI: <https://doi.org/10.1101/gad.2042011>, PMID: 21724832
- Kim N**, Jun MH, Jeong JY, Oh WJ. 2022. Optimized protocol for transcriptome analysis of mouse brain endothelial cells. *PLOS ONE* **17**:e0275036. DOI: <https://doi.org/10.1371/journal.pone.0275036>
- Klingberg A**, Hasenberg A, Ludwig-Portugall I, Medyukhina A, Männ L, Brenzel A, Engel DR, Figge MT, Kurts C, Gunzer M. 2017. Fully automated evaluation of total glomerular number and capillary tuft size in nephritic kidneys using lightsheet microscopy. *Journal of the American Society of Nephrology* **28**:452–459. DOI: <https://doi.org/10.1681/ASN.2016020232>, PMID: 27487796
- Kolodkin AL**, Tessier-Lavigne M. 2011. Mechanisms and molecules of neuronal wiring: A primer. *Cold Spring Harbor Perspectives in Biology* **3**:a001727. DOI: <https://doi.org/10.1101/cshperspect.a001727>, PMID: 21123392
- Kreitzer AC**, Malenka RC. 2008. Striatal plasticity and basal ganglia circuit function. *Neuron* **60**:543–554. DOI: <https://doi.org/10.1016/j.neuron.2008.11.005>, PMID: 19038213
- Kronman H**, Richter F, Labonté B, Chandra R, Zhao S, Hoffman G, Lobo MK, Schadt EE, Nestler EJ. 2019. Biology and bias in cell type-specific RNAseq of nucleus accumbens medium spiny neurons. *Scientific Reports* **9**:8350. DOI: <https://doi.org/10.1038/s41598-019-44798-9>, PMID: 31171808
- Kuo HY**, Liu FC. 2019. Synaptic wiring of corticostriatal circuits in basal ganglia: Insights into the pathogenesis of neuropsychiatric disorders. *eNeuro* **6**:ENEURO.0076-19.2019. DOI: <https://doi.org/10.1523/ENEURO.0076-19.2019>, PMID: 31097624
- Lin J**, Liu J, Wang Y, Zhu J, Zhou K, Smith N, Zhan X. 2005. Differential regulation of cortactin and N-WASP-mediated actin polymerization by missing in metastasis (MIM) protein. *Oncogene* **24**:2059–2066. DOI: <https://doi.org/10.1038/sj.onc.1208412>, PMID: 15688017
- Lin X**, Wang H, Lou Z, Cao M, Zhang Z, Gu N. 2018. Roles of *PIP2* in the membrane binding of MIM I-BAR: insights from molecular dynamics simulations. *FEBS Letters* **592**:2533–2542. DOI: <https://doi.org/10.1002/1873-3468.13186>, PMID: 29995324
- Lobo MK**, Karsten SL, Gray M, Geschwind DH, Yang XW. 2006. FACS-array profiling of striatal projection neuron subtypes in juvenile and adult mouse brains. *Nature Neuroscience* **9**:443–452. DOI: <https://doi.org/10.1038/nn1654>, PMID: 16491081

- Lowery LA**, Van Vactor D. 2009. The trip of the tip: understanding the growth cone machinery. *Nature Reviews. Molecular Cell Biology* **10**:332–343. DOI: <https://doi.org/10.1038/nrm2679>, PMID: 19373241
- Machesky LM**, Johnston SA. 2007. MIM: a multifunctional scaffold protein. *Journal of Molecular Medicine* **85**:569–576. DOI: <https://doi.org/10.1007/s00109-007-0207-0>, PMID: 17497115
- Mata A**, Gil V, Pérez-Clausell J, Dasilva M, González-Calixto MC, Soriano E, García-Verdugo JM, Sanchez-Vives MV, Del Río JA. 2018. New functions of Semaphorin 3E and its receptor PlexinD1 during developing and adult hippocampal formation. *Scientific Reports* **8**:1381. DOI: <https://doi.org/10.1038/s41598-018-19794-0>, PMID: 29358640
- Mattila PK**, Salminen M, Yamashiro T, Lappalainen P. 2003. Mouse MIM, a tissue-specific regulator of cytoskeletal dynamics, interacts with ATP-actin monomers through its C-terminal WH2 domain. *The Journal of Biological Chemistry* **278**:8452–8459. DOI: <https://doi.org/10.1074/jbc.M212113200>, PMID: 12482861
- Minkeviciene R**, Hlushchenko I, Virenque A, Lahti L, Khanal P, Rauramaa T, Koistinen A, Leinonen V, Noe FM, Hotulainen P. 2019. MIM-deficient mice exhibit anatomical changes in dendritic spines, cortex volume and brain ventricles, and functional changes in motor coordination and learning. *Frontiers in Molecular Neuroscience* **12**:276. DOI: <https://doi.org/10.3389/fnmol.2019.00276>, PMID: 31803019
- Miralles F**, Posern G, Zaromytidou AI, Treisman R. 2003. Actin dynamics control SRF activity by regulation of its coactivator MAL. *Cell* **113**:329–342. DOI: [https://doi.org/10.1016/s0092-8674\(03\)00278-2](https://doi.org/10.1016/s0092-8674(03)00278-2), PMID: 12732141
- Morello F**, Prasad AA, Rehberg K, Vieira de Sá R, Antón-Bolaños N, Leyva-Díaz E, Adolfs Y, Tissir F, López-Bendito G, Pasterkamp RJ. 2015. Frizzled3 controls axonal polarity and intermediate target entry during striatal pathway development. *The Journal of Neuroscience* **35**:14205–14219. DOI: <https://doi.org/10.1523/JNEUROSCI.1840-15.2015>, PMID: 26490861
- Moriya J**, Minamino T, Tateno K, Okada S, Uemura A, Shimizu I, Yokoyama M, Nojima A, Okada M, Koga H, Komuro I. 2010. Inhibition of semaphorin as a novel strategy for therapeutic angiogenesis. *Circulation Research* **106**:391–398. DOI: <https://doi.org/10.1161/CIRCRESAHA.109.210815>, PMID: 19940264
- Neuhaus-Follini A**, Bashaw GJ. 2015. The intracellular domain of the frazzled/DCC receptor is a transcription factor required for commissural axon guidance. *Neuron* **87**:751–763. DOI: <https://doi.org/10.1016/j.neuron.2015.08.006>, PMID: 26291159
- O'Donnell M**, Chance RK, Bashaw GJ. 2009. Axon growth and guidance: receptor regulation and signal transduction. *Annual Review of Neuroscience* **32**:383–412. DOI: <https://doi.org/10.1146/annurev.neuro.051508.135614>, PMID: 19400716
- Oh WJ**, Gu C. 2013a. Establishment of neurovascular congruency in the mouse whisker system by an independent patterning mechanism. *Neuron* **80**:458–469. DOI: <https://doi.org/10.1016/j.neuron.2013.09.005>, PMID: 24139045
- Oh WJ**, Gu C. 2013b. The role and mechanism-of-action of Sema3E and Plexin-D1 in vascular and neural development. *Seminars in Cell & Developmental Biology* **24**:156–162. DOI: <https://doi.org/10.1016/j.semcdb.2012.12.001>, PMID: 23270617
- Pecho-Vrieseling E**, Sigrist M, Yoshida Y, Jessell TM, Arber S. 2009. Specificity of sensory-motor connections encoded by Sema3e-Plxn1 recognition. *Nature* **459**:842–846. DOI: <https://doi.org/10.1038/nature08000>, PMID: 19421194
- Penrod RD**, Kourrich S, Kearney E, Thomas MJ, Lanier LM. 2011. An embryonic culture system for the investigation of striatal medium spiny neuron dendritic spine development and plasticity. *Journal of Neuroscience Methods* **200**:1–13. DOI: <https://doi.org/10.1016/j.jneumeth.2011.05.029>, PMID: 21672554
- Percipalle P**, Visa N. 2006. Molecular functions of nuclear actin in transcription. *The Journal of Cell Biology* **172**:967–971. DOI: <https://doi.org/10.1083/jcb.200512083>, PMID: 16549500
- Poliak S**, Morales D, Croteau LP, Krawchuk D, Palmesino E, Morton S, Cloutier JF, Charron F, Dalva MB, Ackerman SL, Kao TJ, Kania A. 2015. Synergistic integration of Netrin and ephrin axon guidance signals by spinal motor neurons. *eLife* **4**:e10841. DOI: <https://doi.org/10.7554/eLife.10841>, PMID: 26633881
- Russell SA**, Bashaw GJ. 2018. Axon guidance pathways and the control of gene expression. *Developmental Dynamics* **247**:571–580. DOI: <https://doi.org/10.1002/dvdy.24609>, PMID: 29226467
- Saarikangas J**, Kourdougli N, Senju Y, Chazal G, Segerstråle M, Minkeviciene R, Kuurne J, Mattila PK, Garrett L, Hölter SM, Becker L, Racz I, Hans W, Klopstock T, Wurst W, Zimmer A, Fuchs H, Gailus-Durner V, Hrabě de Angelis M, von Ossowski L, et al. 2015. MIM-induced membrane bending promotes dendritic spine initiation. *Developmental Cell* **33**:644–659. DOI: <https://doi.org/10.1016/j.devcel.2015.04.014>, PMID: 26051541
- Sakurai A**, Gavard J, Annas-Linhares Y, Basile JR, Amornphimoltham P, Palmby TR, Yagi H, Zhang F, Randazzo PA, Li X, Weigert R, Gutkind JS. 2010. Semaphorin 3E initiates antiangiogenic signaling through plexin D1 by regulating Arf6 and R-Ras. *Molecular and Cellular Biology* **30**:3086–3098. DOI: <https://doi.org/10.1128/MCB.01652-09>
- Sakurai A**, Jian X, Lee CJ, Manavski Y, Chavakis E, Donaldson J, Randazzo PA, Gutkind JS. 2011. Phosphatidylinositol-4-phosphate 5-kinase and GEP100/Brag2 protein mediate antiangiogenic signaling by semaphorin 3E-plexin-D1 through Arf6 protein. *The Journal of Biological Chemistry* **286**:34335–34345. DOI: <https://doi.org/10.1074/jbc.M111.259499>, PMID: 21795701
- Samarakoon R**, Goppelt-Strube M, Higgins PJ. 2010. Linking cell structure to gene regulation: signaling events and expression controls on the model genes PAI-1 and CTGF. *Cellular Signalling* **22**:1413–1419. DOI: <https://doi.org/10.1016/j.cellsig.2010.03.020>, PMID: 20363319
- Scott-Solomon E**, Kuruvilla R. 2018. Mechanisms of neurotrophin trafficking via Trk receptors. *Molecular and Cellular Neurosciences* **91**:25–33. DOI: <https://doi.org/10.1016/j.mcn.2018.03.013>, PMID: 29596897

- Surmeier DJ**, Ding J, Day M, Wang Z, Shen W. 2007. D1 and D2 dopamine-receptor modulation of striatal glutamatergic signaling in striatal medium spiny neurons. *Trends in Neurosciences* **30**:228–235. DOI: <https://doi.org/10.1016/j.tins.2007.03.008>, PMID: 17408758
- Tata A**, Stoppel DC, Hong S, Ben-Zvi A, Xie T, Gu C. 2014. An image-based RNAi screen identifies SH3BP1 as a key effector of Semaphorin 3E-PlexinD1 signaling. *The Journal of Cell Biology* **205**:573–590. DOI: <https://doi.org/10.1083/jcb.201309004>, PMID: 24841563
- Tessier-Lavigne M**, Goodman CS. 1996. The molecular biology of axon guidance. *Science* **274**:1123–1133. DOI: <https://doi.org/10.1126/science.274.5290.1123>, PMID: 8895455
- van der Zwaag B**, Hellemons A, Leenders WPJ, Burbach JPH, Brunner HG, Padberg GW, Van Bokhoven H. 2002. PLEXIN-D1, a novel PLEXIN family member, is expressed in vascular endothelium and the central nervous system during mouse embryogenesis. *Developmental Dynamics* **225**:336–343. DOI: <https://doi.org/10.1002/dvdy.10159>, PMID: 12412018
- Vitriol EA**, Zheng JQ. 2012. Growth cone travel in space and time: the cellular ensemble of cytoskeleton, adhesion, and membrane. *Neuron* **73**:1068–1081. DOI: <https://doi.org/10.1016/j.neuron.2012.03.005>, PMID: 22445336
- Winckler B**, Mellman I. 2010. Trafficking guidance receptors. *Cold Spring Harbor Perspectives in Biology* **2**:a001826. DOI: <https://doi.org/10.1101/cshperspect.a001826>, PMID: 20504966
- Yamashita N**, Usui H, Nakamura F, Chen S, Sasaki Y, Hida T, Suto F, Taniguchi M, Takei K, Goshima Y. 2014. Plexin-A4-dependent retrograde semaphorin 3A signalling regulates the dendritic localization of GluA2-containing AMPA receptors. *Nature Communications* **5**:3424. DOI: <https://doi.org/10.1038/ncomms4424>, PMID: 24599038
- Yamashita N**. 2019. Retrograde signaling via axonal transport through signaling endosomes. *Journal of Pharmacological Sciences* **141**:91–96. DOI: <https://doi.org/10.1016/j.jphs.2019.10.001>, PMID: 31679963
- Yeh ML**, Gonda Y, Mommersteeg MTM, Barber M, Ypsilanti AR, Hanashima C, Parnavelas JG, Andrews WD. 2014. Robo1 modulates proliferation and neurogenesis in the developing neocortex. *The Journal of Neuroscience* **34**:5717–5731. DOI: <https://doi.org/10.1523/JNEUROSCI.4256-13.2014>, PMID: 24741061
- Yu J**, Lin S, Wang M, Liang L, Zou Z, Zhou X, Wang M, Chen P, Wang Y. 2016. Metastasis suppressor 1 regulates neurite outgrowth in primary neuron cultures. *Neuroscience* **333**:123–131. DOI: <https://doi.org/10.1016/j.neuroscience.2016.07.002>, PMID: 27401056
- Yu R**, Kim N-S, Li Y, Jeong J-Y, Park S-J, Zhou B, Oh W-J. 2022. Vascular Sema3E-Plexin-D1 signaling reactivation promotes post-stroke recovery through VEGF downregulation in mice. *Translational Stroke Research* **13**:142–159. DOI: <https://doi.org/10.1007/s12975-021-00914-4>, PMID: 33978913

Appendix 1

Appendix 1—key resources table

Reagent type (species) or resource	Designation	Source or reference	Identifiers	Additional information
Antibody	Anti-Mtss1 (rabbit polyclonal)	Novus Biologicals	Cat# NBP2-24716; RRID:AB_2716709	IHC (1:500) WB (1:500)
Antibody	Anti-Plexin-D1 (goat polyclonal)	R&D Systems	Cat# AF4160; RRID:AB_2237261	IHC (1:500)
Antibody	Anti-Tau (goat polyclonal)	Santa Cruz	Cat# sc-1995; RRID:AB_632467	ICC (1:500)
Antibody	Anti-Neurofilament (mouse)	Hybridoma Bank	Cat# 2H3; RRID:AB_531793	IHC (1:500)
Antibody	Anti- β -actin/HRP (rabbit monoclonal)	Cell Signaling Technology	Cat# 5125S; RRID:AB_1903890	WB (1:5000)
Antibody	Anti-Myc (mouse monoclonal)	Cell Signaling Technology	Cat# 2276; RRID:AB_331783	WB (1:1000)
Antibody	Anti-Vsv (goat polyclonal)	Abcam	Cat# ab3861; RRID:AB_304118	WB (1:1000)
Antibody	Anti-Sema3E (human polyclonal)	LSBio	Cat# LS-c353198	WB (1:500)
Antibody	Anti-Phospho-Akt (rabbit polyclonal)	Cell Signaling Technology	Cat# 9271; RRID:AB_329825	WB (1:1000)
Antibody	Anti-Akt (rabbit polyclonal)	Cell Signaling Technology	Cat# 9272; RRID:AB_329827	WB (1:1000)
Antibody	Anti-RFP (rabbit polyclonal)	Abcam	Cat# ab62341; RRID:AB_945213	IHC (1:1000)
Antibody	Anti-RFP (mouse monoclonal)	Thermo Fisher Scientific	Cat# MA5-15257; RRID:AB_10999796	IHC (1:1000)
Antibody	Anti-alpha-tubulin (mouse monoclonal)	Sigma-Aldrich	Cat# T5168; RRID:AB_477579	IHC (1:1000)
Antibody	Anti-cleaved caspase3 (rabbit polyclonal)	Cell Signaling Technology	Cat# 9661; RRID:AB_2341188	IHC (1:1000)
Antibody	Anti-CD31 (rat monoclonal)	BD Bioscience	Cat# 553370; RRID:AB_394816	IHC (1:500)
Antibody	Anti-digoxigenin-alkaline phosphatase (sheep polyclonal)	Roche	Cat# 11093274910; RRID:AB_2313640	In situ (1:3000)
Antibody	Anti-mouse IgG/HRP (goat polyclonal)	Thermo Fisher Scientific	Cat# 31430; RRID:AB_228307	WB (1:10,000)
Antibody	Donkey anti-rabbit IgG/HRP (rabbit polyclonal)	Jackson Immuno Research	Cat# 711-035-152; RRID:AB_10015282	WB (1:10,000)
Antibody	Donkey anti-goat IgG/HRP (goat polyclonal)	Jackson Immuno Research	Cat# 705-035-147; RRID:AB_2313587	WB (1:10,000)
Antibody	Donkey anti-rabbit IgG, Alexa Fluor 488	Thermo Fisher Scientific	Cat# A-21206; RRID:AB_2535792	ICC (1:1000) IHC (1:1000)
Antibody	Donkey anti-mouse IgG, Alexa Fluor 488	Thermo Fisher Scientific	Cat# A-21202; RRID:AB_141607	ICC (1:1000) IHC (1:1000)
Antibody	Donkey anti-goat IgG, Alexa Fluor 568	Thermo Fisher Scientific	Cat# A-11057; RRID:AB_142581	ICC (1:1000) IHC (1:1000)
Antibody	Donkey anti-rabbit IgG, Alexa Fluor 568	Thermo Fisher Scientific	Cat# A-10042; RRID:AB_2534017	ICC (1:1000) IHC (1:1000)

Appendix 1 Continued on next page

Appendix 1 Continued

Reagent type (species) or resource	Designation	Source or reference	Identifiers	Additional information
Antibody	Donkey anti-mouse IgG, Alexa Fluor 568	Thermo Fisher Scientific	Cat# A-10037; RRID:AB_2757558	ICC (1:1000) IHC (1:1000)
Antibody	Donkey anti-mouse IgG, Alexa Fluor 647	Thermo Fisher Scientific	Cat# A-31571; RRID:AB_162542	ICC (1:1000) IHC (1:1000)
Chemical compound, drug	MK2206	SelleckChem	Cat# S1078	
Chemical compound, drug	TRIzol™ Reagent	Thermo Fisher Scientific	Cat# 15596026	
Chemical compound, drug	RNasin Ribonuclease Inhibitor	Promega	Cat# N2115	
Chemical compound, drug	Halt Protease and Phosphatase Inhibitor Cocktail	Thermo Fisher Scientific	Cat# 78444	
Chemical compound, drug	SuperSignal West Pico PLUS Chemiluminescent Substrate	Thermo Fisher Scientific	Cat# 34580	
Chemical compound, drug	SuperSignal West Femto Maximum Sensitivity Substrate	Thermo Fisher Scientific	Cat# 34096	
Chemical compound, drug	ProLong Diamond Antifade Mountant with DAPI	Thermo Fisher Scientific	Cat# P36962	
Chemical compound, drug	Eukitt Quick-hardening mounting medium	Sigma-Aldrich	Cat# 03989	
Chemical compound, drug	Alexa Fluor 488 Phalloidin	Thermo Fisher Scientific	Cat# A12379	
Chemical compound, drug	Alexa Fluor 568 Phalloidin	Thermo Fisher Scientific	Cat# A12380	
Chemical compound, drug	Alexa Fluor 647 Phalloidin	Thermo Fisher Scientific	Cat# A22287	
Chemical compound, drug	Gibco DMEM, high glucose, pyruvate	Gibco	Cat# 11995-065	
Chemical compound, drug	Penicillin-Streptomycin	HyClone	Cat# SV30010	
Chemical compound, drug	Paraformaldehyde	Electron Microscopy Sciences	Cat# 19202	
Chemical compound, drug	Poly-D-lysine hydrobromide	Sigma-Aldrich	Cat# P6407	
Chemical compound, drug	Corning Laminin	Corning	Cat# 354232	
Chemical compound, drug	NBT/BCIP Ready-to-Use Tablets	Roche	Cat# 11697471001	
Chemical compound, drug	Dil (1.1-dioctadecyl-3,3,3-tetramethylindocarbocyanine perchlorate)	Sigma-Aldrich	Cat# 468495	
Commercial assay or kit	QuantiTect Reverse Transcription kit	QIAGEN	Cat# 205313	
Commercial assay or kit	Pierce BCA Protein Assay Kit	Thermo Fisher Scientific	Cat# 23225	
Commercial assay or kit	Lipofectamine 2000 Transfection Reagent	Thermo Fisher Scientific	Cat# 11668019	
Commercial assay or kit	Basic Nucleofector Kit	LONZA	Cat# VAPI-1003	
Commercial assay or kit	FD Rapid GolgiStain Kit	FD Neurotechnologies Inc	Cat# PK401A	
Cell line (<i>Homo sapiens</i>)	HEK293T Kidney (embryo)	ATCC	CRL-3216; RRID:CVCL_0063	

Appendix 1 Continued on next page

Appendix 1 Continued

Reagent type (species) or resource	Designation	Source or reference	Identifiers	Additional information
Cell line (<i>Cercopithecus aethiops</i>)	COS7 Kidney	Korean Cell Line Bank	Cat# 21651; RRID:CVCL_0224	
Cell line (<i>H. sapiens</i>)	HUVEC Umbilical Vein Endothelial Cells	Lonza	CC-2935; RRID:CVCL_2959	
Cell line (<i>H. sapiens</i>)	HCMEC/D3 Human temporal lobe microvessels	Millipore	SCC066; RRID:CVCL_U985	
Strains	Mouse: C57BL/6J	The Jackson Laboratory	Stock# 000664; RRID:IMSR_JAX:000664	
Strains	Mouse: Nestin-Cre	The Jackson Laboratory	Stock# 003771; RRID:IMSR_JAX:003771	
Strains	Mouse: Tie2-Cre	The Jackson Laboratory	Stock# 008863; RRID:IMSR_JAX:008863	
Strains	Mouse: Drd1a-tdTomato	The Jackson Laboratory	Stock# 016204; RRID:IMSR_JAX:016204	
Strains	Mouse: <i>Mtss1flox/+</i>	Center for Animal Resources and Development Database (CARD) under permission of Dr. Mineko Kengaku	Card ID#2760	
Strains	Mouse: <i>Plxnd1flox/flox</i>	Obtained from Dr. Chenghua Gu	Kim et al., 2011	
Strains	Mouse: <i>Sema3e+/-</i>	Obtained from Dr. Chenghua Gu	Chauvet et al., 2007	
Software, algorithm	ImageJ	NIH	https://imagej.nih.gov/ij/	
Software, algorithm	Prism 9	GraphPad	https://www.graphpad.com/scientific-Software/prism/	
Software, algorithm	Image Lab (v5.2.1)	Bio-Rad	https://www.bio-rad.com/	
Software, algorithm	Fusion FX	Vilber	https://www.vilber.com/fusion-fx/	
Software, algorithm	LightCycler480 (v1.5.1)	Roche	https://lifescience.roche.com/	
Software, algorithm	Leica Application Suite X	Leica	https://www.leicamicrosystems.com/	
Software, algorithm	NIS-Elements AR (v4.51.00)	Nickon	https://www.microscope.healthcare.nikon.com/	
Software, algorithm	NIS-Elements (v4.50.00)	Nickon	https://www.microscope.healthcare.nikon.com/	
Software, algorithm	AIVIA	Aivia, Inc	https://www.aivia-Software.com/	
Other	Immobilon-P PVDF Membrane	Merck	Cat# IPVH00010	
Other	RNA-seq (P5 mice, striatum)	Data and code availability section in this paper	GEO: GSE196558	